



Proton uptake and proton distribution in perovskite materials for protonic ceramic fuel cell applications

Bo Liu,^a Chenzhao Liu,^a Xiaowei Zou,^b Dong Yan,^a  Jian Li,^a Lichao Jia^{a*} 

^a School of Materials Science and Engineering, State Key Lab of Material Processing and Die & Mould Technology, Huazhong University of Science and Technology, Wuhan 430074, China

^b Hubei Institute of Science and Technology Information, Wuhan 430071, China

Protonic ceramic fuel cells can generate electric power directly by converting the chemical energy stored in fuels through electrochemical reactions, offering a great potential for practical applications due to their high efficiency, low emissions and fuel flexibility. Lower and intermediate working temperatures (400–700 °C) are prerequisites for the commercialization, but inefficient proton uptake and the conduction ability of electrolyte and cathode materials limits the output performance. In this review, we summarize the common methods used to detect the proton concentration and distribution in some typical proton-conducting perovskites. The infrared absorption and Raman spectra combined with the first-principle calculations could provide the most information about hydrogen bond types with vibrational frequencies at 1000–4500 cm^{−1}, the local proton environment and interactions between proton and crystal defects. The protons in a symmetric environment are easier to transport in the structure compared with that in an asymmetrical and trapped environment. A good understanding of proton uptake and proton distribution features in perovskite materials is necessary to design suitable proton-conducting materials.

The bibliography includes 167 references.

Contents

| | |
|---|----|
| 1. Introduction | 1 |
| 2. Distribution and effects of protons on the crystal structures | 2 |
| 2.1. Infrared absorption and Raman spectroscopy data | 2 |
| 2.1.1. IR spectroscopy data | 3 |
| 2.1.2. Raman spectroscopy data | 5 |
| 2.2. Neutron scattering method | 7 |
| 2.2.1. Neutron diffraction | 7 |
| 2.2.2. Inelastic neutron scattering | 8 |
| 2.3. Extended X-ray absorption of fine structure | 10 |
| 3. Determination of proton concentration | 11 |
| 3.1. Thermogravimetric analysis | 11 |
| 3.2. Methods of H ₂ O-TPD, PGAA and Karl Fischer titration | 13 |
| 4. Conclusion | 14 |
| 5. List of acronyms and designations | 15 |
| 6. References | 15 |

1. Introduction

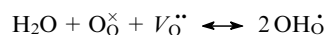
Energy is the cornerstone of the development of science and technology.¹ However, one of the main problems in the 21st century is the energy dilemma.^{2,3} Traditional fossil energy is inefficient and harmful to the environment. Therefore, the development of novel highly efficient, non-polluting and sustainable energy sources has been under the spotlight.^{4,5} Compared with the sources of green energy, such as wind and solar, hydrogen energy can provide more stable power with flexible applications. Furthermore, solid oxide fuel cells (SOFCs) with hydrogen fuel exhibit 90% energy

conversion efficiency, showing great potential as next-generation energy devices.^{6–9}

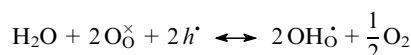
Solid oxide fuel cells can be classified into two types: oxygen ion-conducting SOFCs (O-SOFCs) and protonic ceramic fuel cells (PCFCs),^{10,11} where the main carrier in the electrolyte are oxygen ions in the former and protons in the latter.^{12,13} In PCFCs, protons are generated at the anode, then transferred to the cathode through the electrolyte and finally react with oxygen to form water.^{11,14} Protons theoretically have lower transport activation energy than oxygen ions with a smaller radius and a lower mass;^{15,16} thus, PCFCs could exhibit good output performance at lower and intermediate temperatures (400–700 °C).^{17–19} However, numerous issues with the electrolyte and electrode limits the actual performance, such as the poor densification and electronic conductivity of the electrolyte,^{20–25} chemical and thermal compatibility^{26,27} and low catalytic activity of the cathode material.^{18,28,29} Sintering aids and novel sintering methods have been used to resolve the densification problem, and their effects on proton conductivity were reviewed by Li *et al.*³⁰ and Nur Syafkeena *et al.*³¹ Zvonareva *et al.*³² suggested suitable electrolyte material and external parameters, such as high water partial pressure and low oxygen partial pressure, for consideration to reduce electronic conductivity.

The sufficient proton uptake and transport ability for both the electrolyte and cathode are a key basis for achieving high performance. Perovskite materials (ABO₃) and perovskite-like structures, such as double perovskite (AA'BB'O_{5+δ}), Ruddlesden–Popper perovskite (A_{n+1}B_nO_{3n+1}) and brownmillerite (A_nB_nO_{3n−1}), could

accommodate high proton concentration for the chemical and structural feature.^{33–39} The acceptor doping and defects from A and B sites could create more oxygen vacancies to provide a high proton concentration.^{33,34} The proton is generally absorbed in the hydration reaction



through an oxygen vacancy.^{26,40} Poetzsch *et al.*⁴¹ found that the crystal oxygen can also be an active site to form proton under high oxygen partial pressure through the hydrogenation reaction



Zvonareva *et al.*³² analyzed the effect of the defect structure and external parameters on the proton uptake and proton pumping. The hydrogenation reaction may occur when the electron hole concentration was higher than the oxygen vacancy concentration and the external parameters were high temperature, high oxygen partial pressure and high water partial pressure.²⁹

Although a sufficient proton uptake ability is an important prerequisite to ensure high proton conductivity, the higher proton concentration may be due to the lower proton conductivity in $\text{BaZr}_{1-x}\text{Y}_x\text{O}_3$, where the number of valid proton carriers decreases and the number of trapped protons increases with increasing Y concentration.⁴³ The ideal intrinsically high cubic symmetry and the environment of each oxygen are the same; however, the tortuosity of the BO_6 octahedron from element doping and defects could decrease the crystal symmetry. Therefore, the absorbed proton around the lattice oxygen can be in a different environment with various hydrogen bond strengths. The proton transport is mainly based on the Grotthuss mechanism, *i.e.*, the proton transfer from the oxygen to the neighbouring oxygen followed by reorientation. A stronger hydrogen bond favours the transfer step and unfavours the reorientation step, which requires the cleavage of hydrogen bonds.^{44,45} It is necessary to clarify the distribution of protons in the crystal and valid proton carriers, which contributes to the proton conductivity.

A lot of studies have been carried out on estimating the proton conductivity and designing a high-performance electrode material by element doping, architecture modification, machine learning and high-throughput calculations.^{36,46–49} However, the relationship between the proton distribution in the crystal structure and proton

conductivity was rarely mentioned. Only one publication summarized the origin of trapped protons and their effect on the proton transport.⁵⁰ Estimating the precise amounts of absorbed protons and analyzing the distribution features of protons could establish a relationship between micro-structural information and macro-properties, which is helpful in developing high-performance electrolytes and cathode materials. In this review, Section 2 presents the use of wave spectroscopy method to detect proton signals, and Section 3 suggests a common way to measure the proton concentration.

2. Distribution and effects of protons on the crystal structures

2.1. Infrared absorption and Raman spectroscopy data

Infrared absorption (IR) signals originate from permanent changes in molecular dipoles,⁵¹ while Raman signals originate from induced dipole changes.⁵² The ABO_3 perovskite structure consists of two sublattices: the BO_6 octahedron and the A-cation sublattice. Generally, the Raman signature of the BO_6 octahedron can represent the signature of the main perovskite structure in terms of the molecular model, the ideal cubic structure without defect presents no first-order Raman signal^{51,53,54} but the IR signal exhibits three active vibrational modes: A–(BO_6) stretching, B–O stretching, and O–B–O bending.⁵⁵ When the symmetry is lowered due crystal defects and the tilting of the BO_6 octahedron, the Raman signal can become active and the number of IR signals increases.^{54,56} Different symmetries can present a shoulder, and various configurations of the vibrating units may broaden the band.⁵⁷ Bands below 1000 cm^{-1} in the IR and Raman spectra are usually associated with the main lattice vibrations,⁵⁷ and the O–H vibrational modes in the crystal are of two types: stretching (ν) and bending (δ) ones, where the former occur in the high-frequency region and the latter can be attributed to the host lattice in the low-frequency region.^{58,59} Therefore, the O–H stretching signal is much more obvious in the IR spectrum than in the Raman spectrum, where the latter can also be used to analyze the effect of protons on the crystal structure.^{60–62} Glerup *et al.*⁵⁸ estimated that the vibrational frequency of O–H stretching is around 3550 cm^{-1} in perovskite, according to the empirical correlation of Nakamoto *et al.*⁶³ The IR spectral data on the vibrations of hydrogen bonds reported in the literature^{57–83} are summarized in Table 1.

Bo Liu. Ph.D. in Materials Science, Postdoctoral fellow in Materials Science at the HUST.

E-mail: liubo644@163.com

Current research interests: cathode materials for protonic ceramics solid oxides and SOFC utilization.

Chenzhao Liu. Ph.D. in Materials Science at the same University.

E-mail: lczhust@163.com

Current research interests: material synthesis, metal-supported protonic ceramic solid oxides and oxygen ions conducting solid oxide fuel cell.

Xiaowei Zou. Ph.D. in Chemistry, Engineer at the HBUST.

E-mail: 15827078957@163.com

Current research interests: material testing, new energy industry technology promotion and technology management.

Dong Yan. Ph.D. in Materials Science, Associate Professor, Doctor of Material Science at the HUST.

E-mail: yand@hust.edu.cn

Current research interests: the overall area of performance of industrial size solid oxide fuel cell (SOFC) technology, and its degradation evaluation in long term testing.

Jian Li. Doctor of Metallic Materials, Doctor of Ceramic Engineering, Professor, Head of the Center for Fuel Cell Innovation at the same University.

E-mail: lijian@hust.edu.cn

Current research interests: single cells, stacks and power system of solid oxide fuel cell.

Lichao Jia. Doctor in Materials Science, Professor at the same University.

E-mail: jialc@hust.edu.cn

Current research interests: the development of high-performance electrodes for SOFC, combining theoretical and experimental studies.

Table 1. Results of the IR spectra on the vibrations of hydrogen bonds reported in the literature.

| Sample | Protonation conditions | Wavenumber, cm ⁻¹ | Vibration group | Ref. |
|--|--|------------------------------|-------------------------------|------|
| BaCe _{0.8} Nd _{0.2} O ₃ | D ₂ O–N ₂ , 500 °C | 2300 | ν(O–D) | 58 |
| | | 3000 | ν(O–H) | 58 |
| BaLaIn _{0.9} Nb _{0.1} O _{4.1} | 2% H ₂ O–air, slow cooling from 1000 to 200 °C | 1600 | H ₂ O | 73 |
| | | 1700 | H ₃ O ⁺ | 73 |
| Ba _{0.5} Sr _{0.5} Sc _{0.175} Nb _{0.025} Co _{0.8} O _{3–δ} | 3% H ₂ O–air 700 °C, 10 h | 3394 | ν(O–H) | 74 |
| BaZn _{0.6} Nb _{0.4} O _{3–δ} | 80% H ₂ O–N ₂ | 2500–3700 | ν(O–H) | 68 |
| BaZr _{0.25} In _{0.75} O _{2.75} | 50% H ₂ O, 250 °C, 180 h | 2500–3700 | ν(O–H) | 75 |
| | | 1650 | H ₂ O bend | 75 |
| | | 1900 | ν(O–H) | 75 |
| BaZr _{1–x} Y _x O _{3–δ} | 30% H ₂ O–Ar, 500 °C, 72 h | 2400 | ν(O–H) | 65 |
| | | 2500–3700 | ν(O–H) | 65 |
| | | 4500 | ν(O–H) + δ(O–H) | 65 |
| BaZr _{0.9} Y _{0.1} O _{2.95} | 2% H ₂ O–O ₂ , 600 °C, 24 h | ~1600 | δ(O–H) | 76 |
| | | ~3400 | ν(O–H) | 76 |
| La _{0.9} Ca _{0.1} ErO _{3–δ} | 8% H ₂ –3% H ₂ O–89% N ₂ , 700 °C | 2686 | ν(O–D) | 58 |
| | | 3635 | ν(O–H) | 58 |
| La _{0.6} Sr _{0.4} Co _{0.2} Fe _{0.8} O _{3–δ} | 40% H ₂ O, 550 °C | 3604 | ν(O–H) | 77 |
| PrCo _{0.5} Ni _{0.5} O _{3–δ} | 3% H ₂ O–air, 600 °C, 15 h | 3000–3500 | ν(O–H) | 78 |
| SrCe _{0.95} Y _{0.05} O _{3–δ} | — | 3605 | ν(O–H) | 58 |
| | | 2662 | ν(O–D) | 58 |
| SrSc _{0.175} Nb _{0.025} Co _{0.8} O _{3–δ} | 3% H ₂ O–air, 700 °C, 10 h | 2900–3600 | ν(O–H) | 69 |
| SrZr _{0.9} Ln _{0.1} O ₃ | — | 1400–4000 | Surface protonic species | 70 |
| | | 2500 | ν(O–D) | 66 |
| SrZr _{0.95} Sc _{0.05} O ₃ | — | 3200 | ν(O–H) | 66 |
| | | 3300–3500 | ν(O–H) | 79 |
| Sm _{1.92} Ca _{0.08} Sn ₂ O _{7–δ} | 40% D ₂ O–H ₂ O, 300 °C, 120 h | 2400–2500 | ν(O–D) | 79 |
| | | 2500–3700 | ν(O–H) | 82 |
| Ba _{1.95} In ₂ O _{4.9} F _{0.1} | 2% H ₂ O–air, slow cooling from 1000 to 200 °C | 1000–1500 | δ(O–H) | 82 |
| | | 2800 | ν(O–H) | 73 |
| BaLaInO ₄ | — | 3600 | isolated OH groups | 73 |
| La _{0.995} Nd _{0.005} SrO ₄ | Wet N ₂ , 300 °C, 20 h | 2200–4500 | ν(O–H) | 80 |
| Ba ₃ (Ca _{1.18} Nb _{1.88})O _{9–δ} | H ₂ O–N ₂ –H ₂ , 478 °C | 3330 | ν(O–H) | 58 |
| | | 3640 | ν(O–H) | 58 |
| | | 2428 | ν(O–D) | 58 |
| Ba ₄ Ca ₂ Nb ₂ O ₁₁ | — | 1620 | H ₂ O bend | 81 |
| Ba _{2–0.5x} CaNbO _{5.5–x} F _x (x = 0–0.15) | 2% H ₂ O–air, slow cooling from 1000 to 150 °C | 2900–3500 | ν(O–H) | 83 |

2.1.1. IR spectroscopy data

Karlsson *et al.*^{57, 61, 64, 65, 67} found that the IR spectra of protonated BaZr_{1–x}M_xO_{3–δ} (x = 0–1, M = In, In, Sc, Ga and Y) showed similar results to the vibration signals of hydrogen bonds at about 1900, 2400 and 4500 cm⁻¹, as well as a stronger O–H stretching band from 2500 to 3700 cm⁻¹, which can be divided into four components at 2700 (A), 3100 (B), 3400 (C) and 3600 cm⁻¹ (D), as illustrated in Fig. 1 a.

A pellet sample was pretreated at 600 °C for 1 h *in vacuo* to avoid the possible formation of surface water and then protonated at 250 °C for 198 h under water-saturated oxygen flow. The calculated O–H stretching modes with different local proton environments in BaZr_{1–x}In_xO_{3–δ} (BZI) were presented in Fig. 1 b.⁶⁷ The radii of Y³⁺ (0.9 Å) and In³⁺ (0.8 Å) are larger than that of Zr⁴⁺ (0.72 Å). Therefore, Y and In doping can cause the oxygen and local distortion in the ZrO₆ octahedron. If a proton is in a symmetric environments, such as In–OH–In and Zr–OH–Zr, the O(1)–H distance is the shortest and the O(1)–O(2) distance is the longest, where the O(1) and O(2) atoms are the nearest and the next nearest oxygens close to H. Therefore, the O–H stretching in a symmetric environ-

ment showed a narrow and higher vibrational band (Fig. 1 c). Besides, when the Y concentration increased from 0% to 50%, the relative integrated intensity of the band A obviously gradually increased and that of the bands B and C slightly decreased (Fig. 1 d). Due to the fact that the relative intensity of the peak is positive related to the concentration of the corresponding species, the band A can represent the protons in an asymmetric environment, such as Zr–OH–M. The protons in more symmetrical sites were less displaced. Thus, the bands B and C were assigned to more symmetrical proton sites, such as Zr–OH–Zr.⁶⁵ A stronger hydrogen bond can facilitate the proton transfer step and is unfavourable to the reorientation step, so, a slight doping of Y (≤20%) can remarkably improve the proton concentration and increase the proton conductivity, but higher Y amounts can result in a serious tortuosity of a ZrO₆ octahedron and lots of trapped proton. Therefore, the proton conductivity of BaZr_{1–x}Y_xO₃ had a plateau shape. For protonated BaZr_{1–x}In_xO_{3–x/2} (x = 0.5 and 0.75), Karlsson *et al.*⁶⁴ also found that the relative intensity of the band D for all samples remained almost unchanged and low at a heating temperature from 30 to 350 °C. The distortion of the ZrO₆ octahedron was greatly distributed

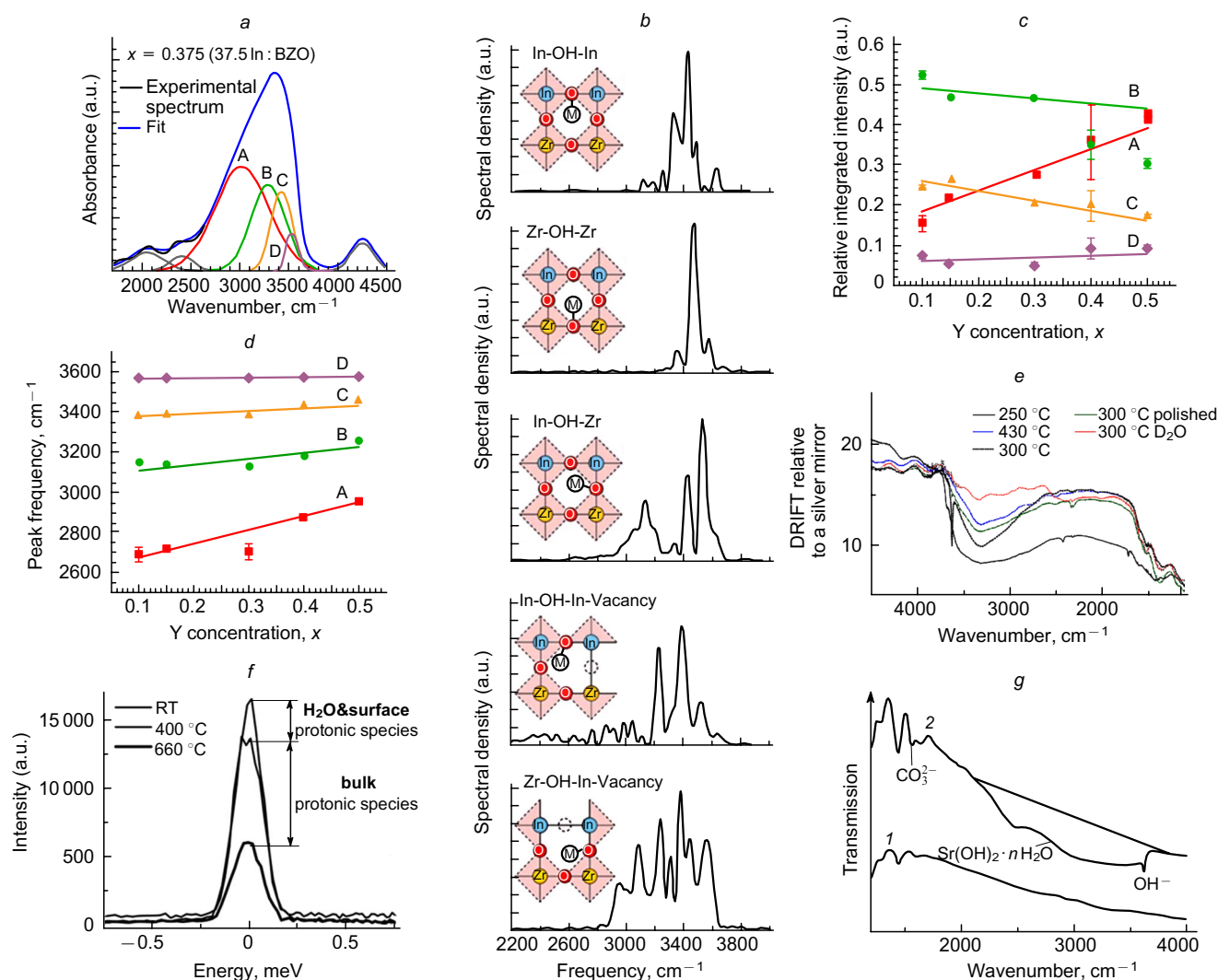


Figure 1. IR spectra of $\text{BaZr}_{0.625}\text{In}_{0.375}\text{O}_{3-\delta}$ together with the fit to seven Gaussians, where the four Gaussians fitted in the range of $2500\text{--}3700\text{ cm}^{-1}$ were marked as A, B, C and D (a).⁶⁵ Reproduced from Ref. 65 with permission from the American Chemical Society. The O–H stretching modes obtained from MD calculations at 300 K with the proton in various local environments (b). Reproduced from Ref. 67 with permission from the American Physical Society. The Y concentration dependence of the relative integrated intensity (c) and the frequency of the peak fitted Gaussians (A, B, C and D) (d). Reproduced from Ref. 65 with permission from the American Chemical Society. The IR spectra of a BCN-18 pellet after equilibration at the indicated temperature, where the sharp peak disappeared upon polishing (e). Reproduced from Ref. 58 with the permission from Elsevier. Elastic scattering neutron spectra of protonated 99% dense $\text{SrZr}_{0.9}\text{Ln}_{0.1}\text{O}_{3-\delta}$ measured at rt, 400 and 660 °C under high vacuum using a time-of-flight spectrometer (f). Reproduced from Ref. 70 with permission from Springer. The IR transmission spectra of very high dense (1) protonated polished ceramics and dense (2) protonated $\text{SrZr}_{0.9}\text{Ln}_{0.1}\text{O}_{3-\delta}$ (g). Reproduced from Ref. 70 with permission from Springer.

in the structure of $\text{BaZr}_{1-x}\text{In}_x\text{O}_{3-x/2}$ ($x = 0.5$ and 0.75) and the number of weak hydrogen bonding sites is quite limited. Therefore, protons were located and strapped at the grain boundaries, with similar values of the concentration of grain boundaries of two samples. The relative intensity of the bands B and C increased while that of the band A decreased for two samples, indicating preferential desorption of protons favored by strong hydrogen bonding. Therefore, the proton involved in strong hydrogen bonding can be mobile under certain force. Yugami *et al.*⁶⁶ also observed the trapped O–H bond at $\sim 3300\text{ cm}^{-1}$ in the protonated $\text{SrZr}_{0.95}\text{Er}_{0.05}\text{O}_{3-\delta}$ (SZE). A single-crystal SZE sample was firstly treated at 750 °C and wet air (58 vol.% H_2O) until the defect was equilibrated, then annealed at 750 °C under dry air for various periods of time, and finally quenched to room temperature, after which the signal of the hydrogen

bond was detected. The IR spectra showed two wide O–H active bands at 3200 and 2500 cm^{-1} , which can be divided into four bands centred at 3300 (A), 3050 (B), 2700 (C) and 2300 cm^{-1} (D), where the intensity of the band A was almost unchanged and those of the other bands obviously decreased when the annealing time increased from 38 to 530 min. In addition, the trapped proton possibly came from the interaction between the proton and the dopant ion,⁶⁶ which resulted in the difficulty of long range diffusion of protons, the proton conductivity being not in proportion to the proton concentration of $\text{SrCe}_{1-x}\text{Yb}_x\text{O}_3$.⁸⁴

The IR signals were also used to predict the proton conductivity of novel electrolyte materials and to prove the proton uptake capacity of triple conducting cathode materials of protonic ceramic solid cells. Arai *et al.*⁶⁸ reported the IR spectra of protonated $\text{Ba}(\text{Zn}_{0.4}\text{Nb}_{0.6})\text{O}_{3-\delta}$ (BZN)

and $\text{Ba}(\text{Zr}_{0.9}\text{Y}_{0.1})\text{O}_{2.95}$ (BZY91). The spectra showed a wide band at $2500\text{--}3700\text{ cm}^{-1}$, which can be divided into four bands centred at 3550, 3500, 3350 and 3100 cm^{-1} . The bands at 3550 and 3500 cm^{-1} were attributed to the symmetrically configured proton sites (denoted as SC), while the other bands to those with asymmetric configuration (denoted as AC). The high relative intensity of the AC site for BZN was obtained in the annealed sample compared with the protonated sample and at a high temperature in the protonated sample. Therefore, the protons at the SC sites were not trapped and acted as valid mobile carriers. Furthermore, protonated BZN had its own higher concentrations of protons at the SC sites compared with BZY, indicating higher proton conductivity for BZN. Zhu *et al.*⁶⁹ found that bands at 2900 and 3600 cm^{-1} were observed for the protonated $\text{SrSc}_{0.175}\text{Nb}_{0.025}\text{Co}_{0.8}\text{O}_{3-\delta}$ (SSNC), which are absent for the dry SSNC sample, suggesting that SSNC was a proton-conducting oxide.

The signals of the surface proton species cannot be neglected in the IR analysis. Glerup *et al.*⁵⁸ also observed the simultaneous presence of surface and bulk protons in protonated $\text{Ba}_3(\text{Ca}_{1.18}\text{Nb}_{1.82})\text{O}_{9-\delta}$ (BCN-18). The band at 3630 cm^{-1} disappeared after the sample pellet was polished, indicating that the surface layer was hydrolyzed (Fig. 1e). Furthermore, when the treating gas of BCN-18 bar changed from $\text{D}_2\text{O}-\text{N}_2$ –air to 8% H_2 –3% H_2O –89% N_2 for 2 h at 480°C , the IR signal of the internal fracture surface of BCN-18 was acquired. The bulk O–D and O–H stretching bands were observed at 2428 and 3330 cm^{-1} , respectively, and the relative intensity of O–D was higher at the center of the bar compared with the place near the surface, indicating the H/D change in the bulk. Interestingly, Slodczyk *et al.*⁷⁰ attributed the wide band between $1400\text{--}4000\text{ cm}^{-1}$ to the signals of the surface proton species $\text{M}^{n+}(\text{H}_2\text{O})_n$. The authors prepared two kinds of $\text{SrZr}_{0.9}\text{Ln}_{0.1}\text{O}_{3-\delta}$ (SZL91) sample with 94% and 99% densities, and all samples were protonated at 500°C under 80 bars of H_2O for few days, the IR signal was collected before and after polishing the protonated sample. They confirmed that the ratio of the surface proton species was extremely low on the surface of the protonated 99% dense SZL91 according to the elastic neutron scattering spectrum (Fig. 1f), whereas there was no band at $1400\text{--}4000\text{ cm}^{-1}$ in the IR spectrum (Fig. 1g). However, upon protonation of the 94% dense SZL91 with a higher surface area attracting the proton, the wide band was observed, similar to the signal of $\text{M}^{n+}(\text{H}_2\text{O})_n$ species.⁷¹ Furthermore, no signal for the O–H stretching band was detected in the polished protonated 99% dense SZL91 sample. The proton in the protonated SZL91 was considered as the ionic proton. Such protons were presented by interstitial protons, free of any specific strong hydrogen bonding, and were first observed in MnO_2 .⁷² The proton uptake ability of SZL91 materials was much lower than that of $\text{BaZr}_{1-x}\text{M}_x\text{O}_{3-\delta}$ at 500°C .⁸⁵ Therefore, the hydroxyl moiety easily formed at the surface of SZL91 and the bulk concentration of hydroxyl was much lower and, consequently, the polished SZL91 presented no vibration signals. Besides, the complex distribution of hydroxyl groups in $\text{BaZr}_{1-x}\text{M}_x\text{O}_{3-\delta}$ leads to a similar wide band at $1400\text{--}4000\text{ cm}^{-1}$ in the IR spectrum.

2.1.2. Raman spectroscopy data

Raman signals were used to determine the type, concentration and distribution of protons in the lattice, especially when combined with the first-principle calculations. Glerup

*et al.*⁵⁸ reported that protonated $\text{La}_{0.9}\text{Ca}_{0.1}\text{ErO}_3$ gave one narrow band at 3618 cm^{-1} , indicating that the proton occupied one site in this material. Furthermore, thermal broadening of the band was observed, where both the intensity and frequency of the O–H vibration decreased and then went back to the original site as the temperature increased from 30 to 200°C and decreased back to 30°C . Bielecki *et al.*⁸⁶ found that protonated $\text{Ba}_2\text{In}_2\text{O}_5$ (BIO) gave a wide asymmetrical band in the range from 2800 to 3800 cm^{-1} , which can be divided into six bands centred at 3050 (I), 3310 (II), 3470 (III), 3540 (IV), 3410 (V) and 3570 cm^{-1} (VI). These six bands were further classified into two proton types, which both occupied the 32y and 4h sites, as shown in Fig. 2a, with the calculated Raman spectra, where type 1 (Martinez 1) was the narrower and strong O–H bond with bands II, III, IV, and VI, and type 2 (Martinez 2) with band V was the weak O–H bond related to the host lattice. In addition, type 1 represented the dominant species ($\sim 75\%$), as calculated by the peak intensity. Furthermore, the deprotonation rate was the same for protons of all types and sites at 370°C . However, the dissociation rate at 4h was higher than that at 32y for type 1 and was equal for type 2 at a temperature above 400°C . Therefore, type 2 almost disappeared at high temperatures. The proton at 32y for type 1 is located in a non-centrosymmetric distorted environment of the InO_6 octahedron, which means that hydrogen bonds at the 32y site of type 1 are thermally stable. Mazzei *et al.*³⁵ further found that elements doping with 15 mol.% M (M = Ga, Sc, Y) in the B site of BIO could effectively increase the ratio of type 1 and proton conductivity, and for a small fraction of type 2 could form unusual stronger bond and hinder the proton transport.⁸⁷ However, there was no relationship between the ratio change and ionic radius of the doped element, and the effect of cation substitution on local structural distortions and position sites is much complex. Gao *et al.*⁸⁸ used the change in the intensity ratio of O–D to O–H with time for a $\text{BaZr}_{0.1}\text{Ce}_{0.7}\text{Y}_{0.1}\text{Yb}_{0.1}\text{O}_{3-\delta}$ (BZCYYb) sample to calculate the surface exchange coefficients ($k_{\text{H/D}}$) when the atmosphere changed from 3% H_2O –Ar to 3% D_2O –Ar (Fig. 2b). It was found that $k_{\text{H/D}}$ of nanocrystalline BZCYYb was much higher than that of conventional sol–gel BZCYYb, suggesting that the nanocrystalline BZCYYb membranes had a better proton transport ability. Hua *et al.*⁸⁹ reported that there were no bands at 3500 and 1060 cm^{-1} , which can be assigned to O–H and $-\text{CO}_3$ vibrations, respectively, in $(\text{PrBa}_{0.85}\text{Ca}_{0.15})_{0.5}(\text{MnFe})_{0.5}\text{O}_{3\pm\delta}$ after 1000 cycles of cyclic voltammetry stability tests, which were obvious in $\text{PrBaMnFeO}_{5+\delta}$. Therefore, this proved that a small amount of Ca doping can enhance the stability of $\text{PrBaMnFeO}_{5+\delta}$.

Protonation affects the structural symmetry of materials in different ways. Slodczyk *et al.*⁹¹ reported that the protonation had an opposite effect on the symmetry of $\text{SrZr}_{0.9}\text{Y}_{0.1}\text{O}_3$ (SZYb91) and $\text{Sr}_{0.5}\text{Ba}_{0.5}\text{Ti}_{1-x}\text{Al}_x\text{O}_{3-\delta}$ (SBTAI). For SZYb91, the oxygen vacancy was completely occupied by protons, resulting in an upshift of the characteristic band for the longer and protonated O–Zr bond, with a broadening of the Raman lines and reduction of peak splitting for increased symmetry. By contrast, protons can further increase the torsion of the crystal structure for SBTAI as the low toleration with a proton,⁹² resulting in a downshift of the Ti–O stretching band, evident splitting and the appearance of additional modes. Grimaud *et al.*⁹⁰ revealed that incorporated protons in BZY91 did not

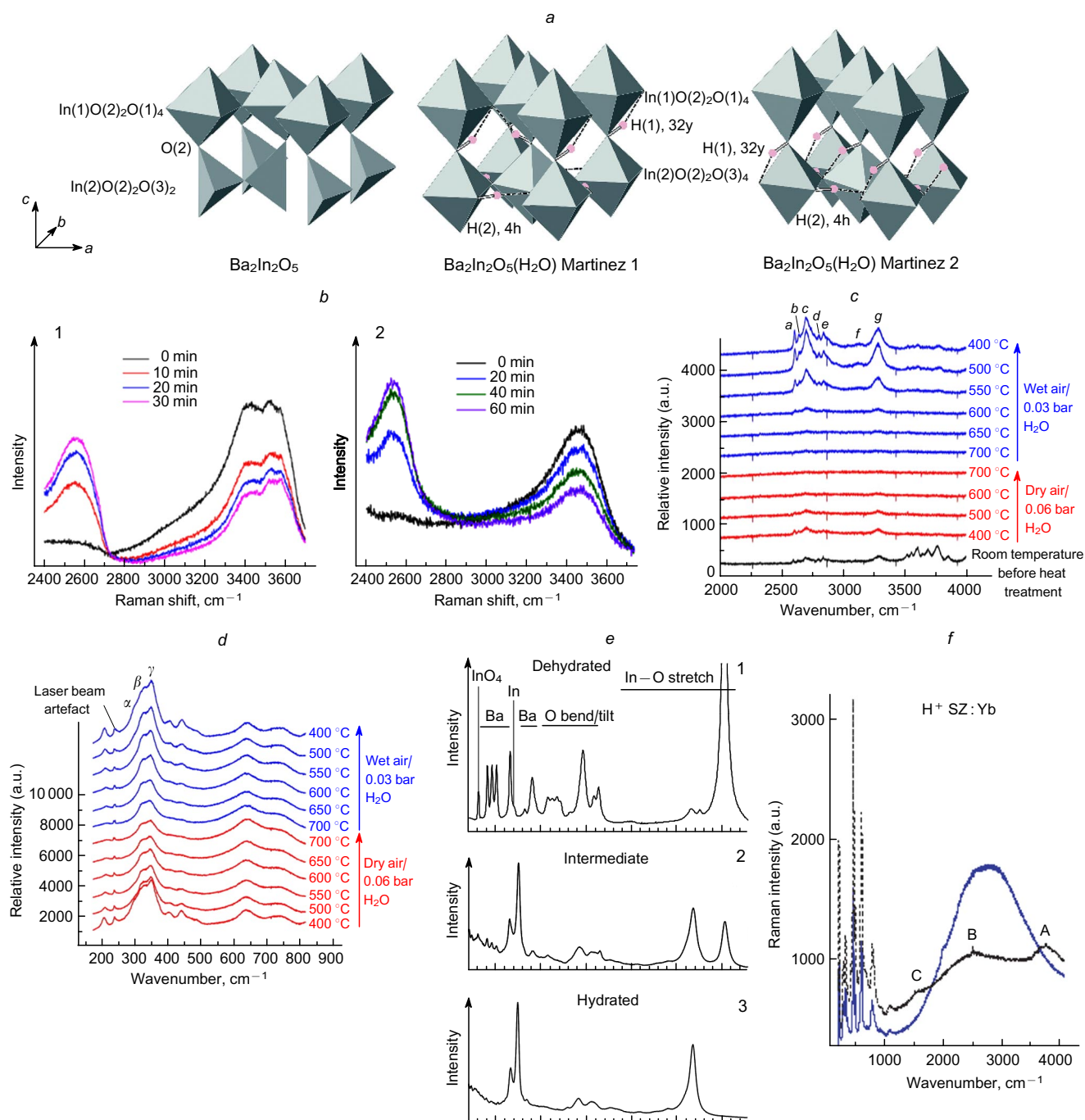


Figure 2. Schematic illustration of the Ba₂In₂O₅ structure and the two lowest-energy proton configurations in BaInO₃H (a). Reproduced from Ref. 86 with permission from the Royal Society of Chemistry. Temporal evolution of Raman spectra of the nanostructured BCZYb membrane (1) and the conventional BCZYb membrane (2) after switching the atmosphere from Ar–3% H₂O to Ar–3% D₂O at 300 °C (b). Reproduced from Ref. 88 with the permission from Wiley. Thermal evolution of Raman spectra recorded on a dense BCY10 pellet at 2000–4000 cm⁻¹ (c) and 160–800 cm⁻¹ (d) under dry and wet air. Reproduced from Ref. 90 with permission from Elsevier. Raman spectra as measured at 20 °C for the dehydrated (1), intermediate (2) and hydrated (3) phases of Ba₂In₂O₅ (e). Reproduced from Ref. 86 with permission from the Royal Society of Chemistry. Raman spectra characteristic of protonated SZYb91 recorded at 532 and 632 nm wavelengths (f). Reproduced from Ref. 91 with permission from Wiley.

significantly affect the crystal structure and the hydrogen bonds had a complex coupling pattern with the lattice at low temperatures. When the dry BZY91 pellet was cooled down from 700 to 400 °C under 3% H₂O–air, the Raman spectra showed three band ranges representing OH vibrations (2600–2900 (a–e), 3100–3350 (f, g) and 3500–3900 cm⁻¹) (Fig. 2 c), three bands representing the

framework vibrations at 300–400 cm⁻¹ (α, β and γ) (Fig. 2 d), and the frequencies of all bands were almost unchanged. In addition, the intensities of β and γ in the protonated sample were higher than those of the dry sample, indicating that protons were incorporated into the bulk of the material. Furthermore, Bielecki *et al.*⁸⁶ found that the hydration could lead to a phase change in BIO from

brownmillerite to a perovskite-like structure. Compared with the signal of In–O in the dry and protonated samples, the intensity of the band at 600 cm^{-1} , which was assigned to In–O stretching in the InO_4 tetrahedra, gradually decreased and finally disappeared. At the same time, the intensity of band at 530 cm^{-1} increased, representing the O–In stretching of the InO_6 octahedra as shown in Fig. 2e.

In some materials, the pressure and fluorescence can affect the Raman signal. Slodczyk *et al.*⁹³ studied the effect of pressure from 0 to 40 GPa in protonated $\text{SrZr}_{0.93}\text{Y}_{0.07}\text{O}_{3-\delta}$ (SZY93). The peak at 750 cm^{-1} corresponding to the ZrO_6 vibration broadened and became less intense after hydration, while peak splitting at 280 and 410 cm^{-1} decreased, indicating lattice shrinkage. The wavenumber of the protonated sample increased slightly with increasing pressure. The lattice vibration signal was observed at a low wavenumber (90, 150 and 175 cm^{-1}), while the Zr–O bending signal occurred at $300\text{--}500\text{ cm}^{-1}$, and the Zr–O modes of an octahedron with/or perturbed by oxygen vacancies and/or proton species appeared at 750 and 755 cm^{-1} . The first-order phase transition, which occurred as the peak at about 750 and 90 cm^{-1} representing orthorhombic symmetry, disappeared at 10 GPa, while the second phase transition to the Imma space group, occurred as the peak at 750 cm^{-1} , was observed again at 20 GPa. In addition, the third phase transition to the tetragonal space group occurred when two peaks at 150 and 175 cm^{-1} fused into one, and a peak at 750 cm^{-1} disappeared again at 35 GPa, which was the result of a coupling between the vacancy/Yb local order and long-range Sr sublattice. Finally, the sample had a cubic phase at 40 GPa. Slodczyk *et al.*⁹¹ tested the Raman signals of protonated SZY91 using 532 and 632 nm wavelengths, as shown in Fig. 2f, where the background shifted down to 632 nm, indicating fluorescence. However, the background was wider than that reported by Boyer *et al.*,⁹⁴ and the researchers thought this was due to the presence of the ABC bands in the structure, which came from different couplings, mechanical and electrical, of the very light H vibrators with all other vibrators of the matter and showed complex mountain-like peaks.⁹⁵

2.2. Neutron scattering method

Neutron scattering can effectively distinguish light elements for interactions between the neutrons, as the nucleus does not increase regularly with an increase in atomic number.^{96,97} Key information, such as crystal symmetry,^{98–100} proton concentration and position,^{101–104} and hydrogen bond strength^{105–108} can be obtained by neutron technology, which can be further divided into three main methods,^{96,109} namely, neutron diffraction (ND), quasi-elastic neutron scattering (QENS) and inelastic neutron scattering (INS). Neutron diffraction technique provides information about the crystal structure of the material, while the proton position in the lattice and the hydrogen bond strength can be obtained by comparing the changes in the diffraction peaks of the material before and after hydration.^{76,80} The difference in the hydrogen bond strength of oxygen in each direction has been further used to analyze the structure distortion in the short range and proton transport.⁸¹ Quasi-elastic neutron scattering is used to study the rotation and picosecond transport of protons between local oxygen atoms, as well as long-range transport in the nanosecond interval.^{107,112,113} Inelastic neutron scattering was shown to acquire the neutron vibrational spectra that allowed for the study of the local structure of the

material, vibrational dynamics and all vibrational modes of hydrogen bonding, including bending and stretching.^{59,59,114,115}

2.2.1. Neutron diffraction

Kendrick *et al.*¹¹⁶ tested protonated $\text{La}_{0.6}\text{Ba}_{0.4}\text{ScO}_{2.8}$ using 3% $\text{H}_2\text{O}-\text{N}_2$ and 3% $\text{D}_2\text{O}-\text{N}_2$ at $500\text{ }^\circ\text{C}$ for 16 h. The neutron diffraction pattern showed the presence of Sc_2O_3 impurities, and, according to the energy-dispersive X-ray spectroscopy (EDX) data, a La : Ba ratio was 0.73 : 0.27 due to barium volatility at high temperatures required for the synthesis of this phase, which was not detected by XRD. The uptake masses of H_2O and D_2O were 1.33 and 1.37, respectively, according to thermogravimetric analysis (TGA), which measured the fully occupied oxygen vacancy. The protonation could increase octahedral tilting when the intensity of d111 and value of d112/d211 increased. The proton and deuteron positions were around O1 (Fig. 3a), with the ab plane pointing toward lanthanum according to Fourier nuclear density analysis.

Malavasi *et al.*¹¹⁰ reported on the neutron diffraction data for BaCeO_3 (BCO) and $\text{BaCe}_{0.9}\text{Y}_{0.1}\text{O}_{2.95}$ (BCY91). For BCO, it consisted of the Pmcn space group, and the ND peak was almost similar for the dry and wet material, as there was no oxygen vacancy for the uptake of H_2O . When BCO was doped with Y, the crystal symmetry was lowered due to the creation of oxygen vacancies, rather than the difference in the ionic radii between Y and Ce. The symmetry of protonated BCY91 could increase after the oxygen vacancy was occupied by the hydroxy group, where O1 was fully occupied and the O_2 site had an occupancy of 0.92 (Fig. 3b).⁹⁷ Eriksson Andersson *et al.*¹¹¹ studied the effect of D_2O on the crystal structure of $\text{BaCe}_{0.8}\text{Y}_{0.2}\text{O}_{3-\delta}$ at elevated temperatures. Dry $\text{BaCe}_{0.8}\text{Y}_{0.2}\text{O}_{3.78}$ presented two phase transitions from $Pm\bar{3}m$ to $R\bar{3}c$ at $775\text{ }^\circ\text{C}$ and from $R\bar{3}c$ to Imma at $250\text{ }^\circ\text{C}$ during cooling from 900 to $100\text{ }^\circ\text{C}$ (Fig. 3c), where the former resulted from stabilization of the antiphase tilting of the $(\text{Ce/Y})\text{O}_{6-\delta}$ units and the latter arose due to the loss of one antiphase tilting. When 20% D_2O was introduced, the presence of the D–O bond could expand the crystal volume and enhance the tendency of tilting either *via* hydrogen bonding interactions or changes in the local electrostatic environment, resulting in the first change temperature increasing to $925\text{ }^\circ\text{C}$ and the new space group Imma appeared at $650\text{ }^\circ\text{C}$. The slower kinetics of proton diffusion at low temperatures could also lead to chemical inhomogeneities when a new phase $I\bar{2}m$ formed at $250\text{ }^\circ\text{C}$. Furthermore, protons can be found in the BCYO perovskite at high temperature, and it was estimated that O–H bonds could take over around 70% oxygen vacancies under 30% $\text{H}_2\text{O}-\text{air}$ at $800\text{ }^\circ\text{C}$.

Basbus *et al.*¹¹⁷ studied the phase transition and proton transport mechanism of $\text{BaCe}_{0.4}\text{Zr}_{0.4}\text{Y}_{0.2}\text{O}_{3-\delta}$ (BZCY442) *via* the *in situ* neutron diffraction. BZCY442 had a rhombohedral symmetry with an $R\bar{3}c$ structure between rt and $400\text{ }^\circ\text{C}$ and cubic symmetry with $Pm\bar{3}m$ above $600\text{ }^\circ\text{C}$. When D_2O was incorporated into the oxygen vacancy, the crystal structure became more stable. The deuterated BZCY442 presented $R\bar{3}c$ at $100\text{--}600\text{ }^\circ\text{C}$ and $Pm\bar{3}m$ at above $600\text{ }^\circ\text{C}$, where the occupancy of D was 0.0334 ($T < 400\text{ }^\circ\text{C}$), 0.0293 ($T = 400\text{--}600\text{ }^\circ\text{C}$) and almost 0 at $T > 700\text{ }^\circ\text{C}$. In the range of $500\text{--}600\text{ }^\circ\text{C}$, the BZCY442 structure shranked, and the cubic intra-octahedral O–O distance occurred during the second order phase transition, where the larger O–O distance and the shorter distance in

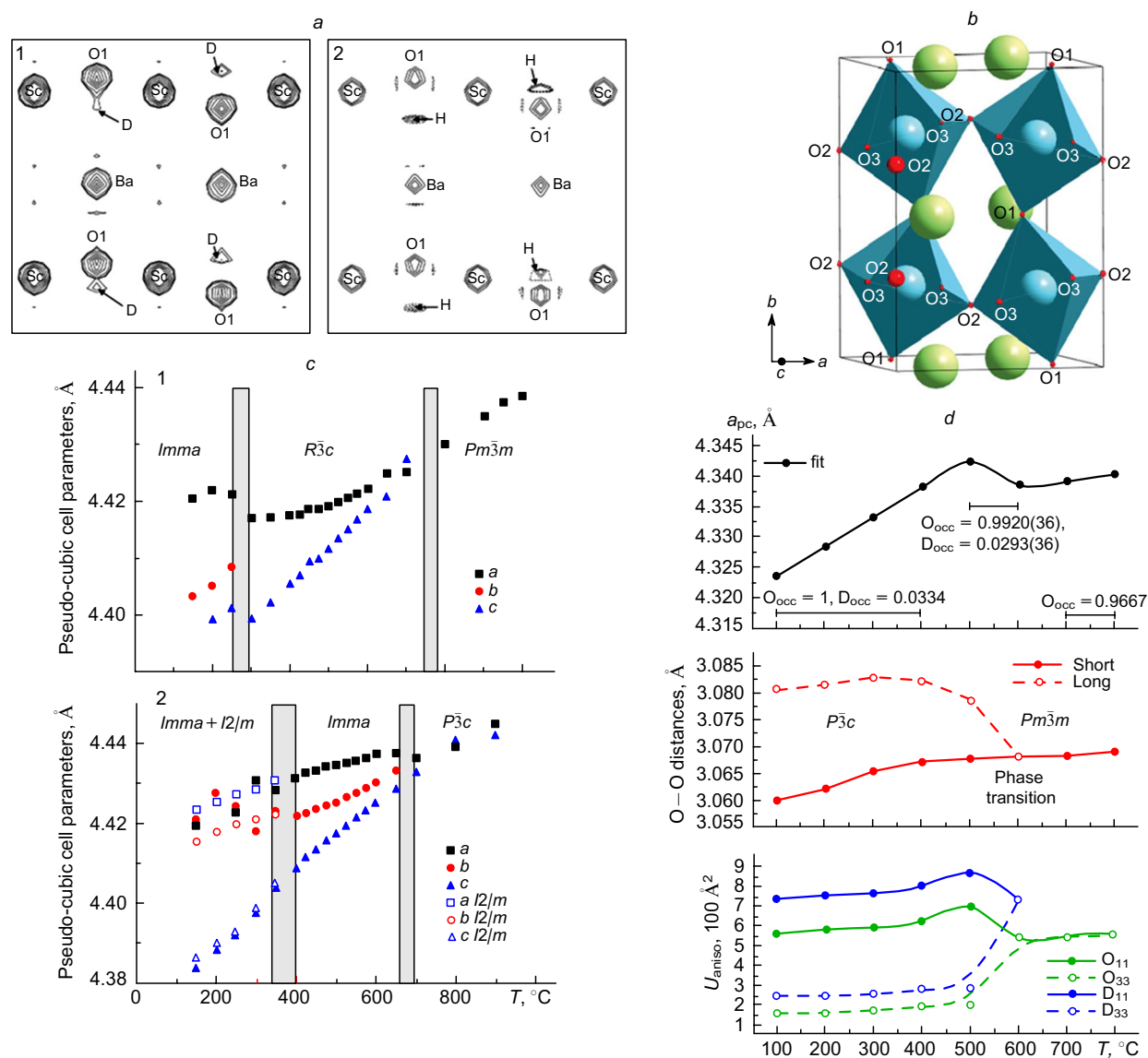


Figure 3. Fourier nuclear density maps obtained from the neutron diffraction data of the ab plane distance (10 Å), where c is 0 Å, showing the presence of (1) deuterium and (2) hydrogen associated with the oxygen atom O1 (a). Reproduced from Ref. 116 with permission from Elsevier. Sketch of the BCY20 crystal structure. Reproduced from Ref. 97 with permission from the American Chemical Society (b). Phase stability fields and pseudo-cubic lattice parameters of BCY20 in the (1) dry O₂ and (2) O₂ + D₂O(g) (c). Reproduced from Ref. 111 with permission from the Royal Society of Chemistry. Temperature dependence of the relevant crystallographic parameters obtained from the neutron powder diffraction data refinement (d). Reproduced from Ref. 117 with permission from the Royal Society of Chemistry.

the rhombohedral symmetry merged into an intermediate distance (Fig. 3 d). Furthermore, the anisotropic displacement (U_{aniso}) parameters of D calculated from the ND data increased up to 500 °C (Fig. 3 d), indicating an increase in the transport ability of the deuterium ion. The structural water desorbed gradually, and the deuterium transport number decreased as well as the oxygen transport number increased at above 400 °C, resulting in the maximum proton conductivity at 600 °C and the oxygen–ionic conductivity dominating at above 600 °C.

2.2.2. Inelastic neutron scattering

Karmonik *et al.*¹⁰⁴ found that the band of the O–H bond of protonated $\text{SrCe}_{0.95}\text{M}_{0.05}\text{O}_{3-\delta}$ (M = Sc, Ho, Nd) occurred at 90–185 meV (1 meV = 8.065 cm^{−1}). Interestingly, a peak also was observed for protonated SrZrO_3 , indicating the presence of intrinsic defects in an undoped

sample. The band intensity of O–H at 112 meV for $\text{SrCe}_{0.95}\text{M}_{0.05}\text{O}_{3-\delta}$ decreased as the temperature increased from −253 to 127 °C, meaning that the depletion of H occurred at low temperatures. Slodczyk *et al.*⁴⁷ found no hydrogen bond in the bulk of protonated $\text{BaZr}_{0.9}\text{Yb}_{0.1}\text{O}_{3-\delta}$ (BZYb91) and $\text{SrZr}_{0.9}\text{Yb}_{0.1}\text{O}_{3-\delta}$ (SZYb91). The bulk proton concentration was 3×10^{-3} and 1×10^{-3} mol mol^{−1} for BZY91 and SZY91, respectively. However, the proton signal was found at ~11 meV in the INS spectrum and no band was found at 3600 cm^{−1} in the IR spectrum. Therefore, the incorporated protons did not combine with the oxygen atoms, but existed solely as an ionic proton, polaronic proton and gas of proton. Ionic protons were also found in BaTiO_3 , and the hydride ions could turn into proton–occupied oxygen vacancies, when the electrons were attracted by the adjacent Ti ions.^{118–120} However, hydrogen bonds were possibly present at the protonated

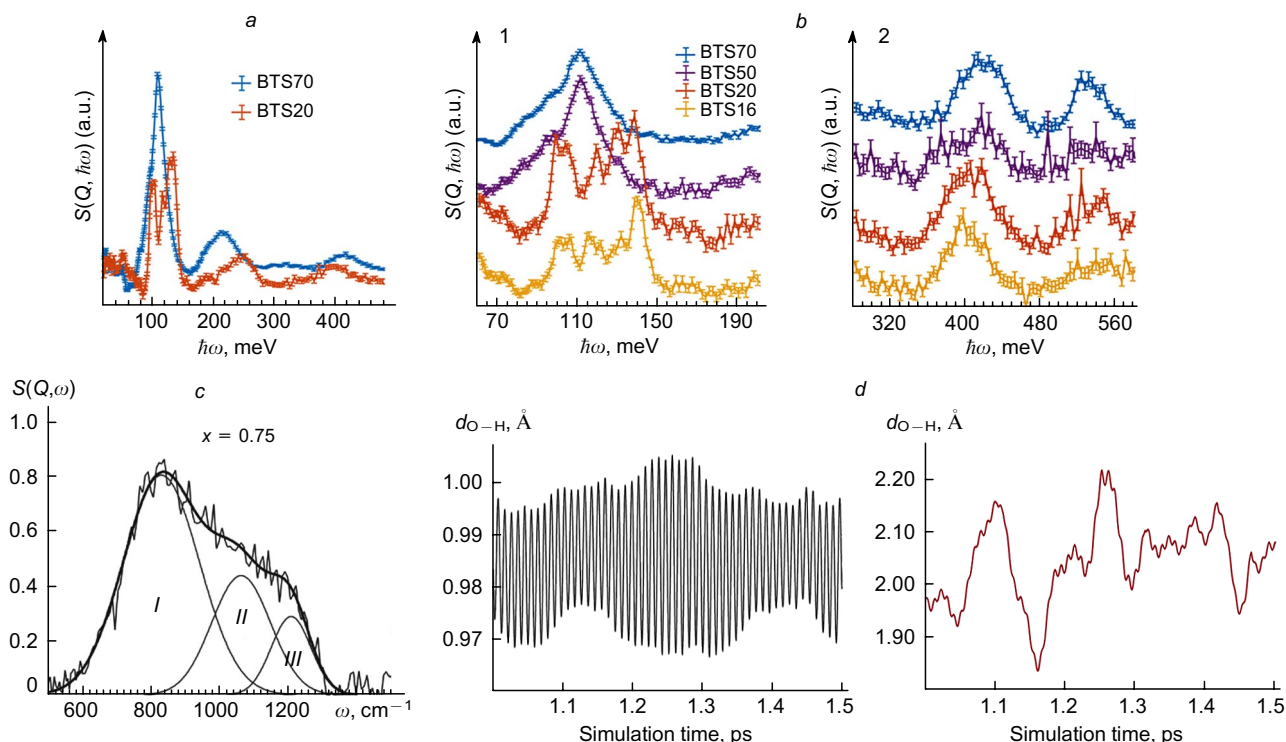


Figure 4. IN1 Lagrange data of $S(Q, \hbar\omega)$ of BTS70 (blue) and BTS20 (red) (a).⁶² The data for the sample obtained on a TOSCA indirect-geometry spectrometer over the $\delta(\text{O}-\text{H})$ (1) and the $\nu(\text{O}-\text{H})$ mode regions (2) (b). Reproduce from Ref. 62 with permission from the American Chemical Society. The Gaussian fit of the baseline corrected O–H wag band for hydrated $\text{BaZr}_{0.25}\text{In}_{0.75}\text{O}_{2.625}$ (c). Reproduced from Ref. 59 with permission from the American Physical Society. Fluctuations of the covalent bond length ($d_{\text{O}-\text{H}}$) and the hydrogen bond length ($d_{\text{O}\cdots\text{H}}$) (d). Reproduce from Ref. 114 with permission from the Royal Society of Chemistry.

$\text{BaTi}_{1-x}\text{Sc}_x\text{O}_3$ ($0.16 < x < 0.7$).⁶² The $\nu(\text{O}-\text{H})$ band was located at 383–443.5 meV, while the band and overtone of $\delta(\text{O}-\text{H})$ were at 90–120 and 190–240.5 meV, respectively (Fig. 4a,b), which can be divided into bands at 98, 104, 118, 128 and 138 meV. Most of these were mainly contributed to the inter-octahedral proton with the bond angle closest to 180° and minor to the proton on the edge of the octahedron. With increasing Sc content, the hexagonal structure gradually decreased and almost turned into a cubic phase at $x = 0.5$, resulting in the formation of a new band at 887 cm⁻¹. In addition, the hydrogen bonds weakened as the energy transfer of $\nu(\text{O}-\text{H})$ increased and that of $\delta(\text{O}-\text{H})$ decreased. Therefore, the higher proton conductivity with high Sc content provided high symmetry and multiple proton sites in the cubic structure.

Karlsson *et al.*⁵⁹ used INS to study the proton positions in $\text{BaZr}_{1-x}\text{In}_x\text{O}_{3-x/2}$ ($x = 0.2-0.75$) and revealed the proton transport type for proton conductivity. The band for O–H bending vibrations appeared at 600–1200 cm⁻¹ and can be divided into three bands at 850 (I), 1070 (II) and 1250 cm⁻¹ (III) as shown in Fig. 4c for $x = 0.75$. Furthermore, an overtone of the fundamental O–H bending band was observed at 1700 cm⁻¹, with similar sharp O–H bending. The O–H bending and stretching vibrations were coupled in BZI, where the decrease in the stretching vibrational frequencies was accompanied by an increase in bending vibrations, and their total wavenumber was at 4100–4300 cm⁻¹. The In atom and oxygen vacancy in the nonsymmetric configurations of protons can push the protons to the neighboring oxygen, and a strong hydrogen bond (O–H \cdots O) can form. Therefore, protons at the local distortion site by In doping can form even stronger hydro-

gen bonds, which can be attributed to bands II and III. With increasing the In content from 20% to 75%, the proton concentration is tripled, similar to the tendency of bulk proton conductivity, where the absolute intensity of band I increased approximately by a factor of two while that of bands II and III, by a factor of 10. Therefore, a weak hydrogen bond was the main mobile phase in the protonated BZI, which was consistent with the Raman spectra data.¹²¹ Mazzei *et al.*^{114,122} reported similar results. The $\delta(\text{O}-\text{H})$ band appeared at 645.2–1209 cm⁻¹ in protonated $\text{BaZr}_{0.5}\text{In}_{0.5}\text{O}_{2.9}$, while the $\nu(\text{O}-\text{H})$ band was found at 2016, 2338, and 2882–3629 cm⁻¹. The stronger $\nu(\text{O}-\text{H})$ bands at 2016 and 2338 cm⁻¹ originated from the distortion of the BO_6 octahedron enhanced by oxygen vacancies or In doping, and paired proton effects, where the proton could be directly affected by another proton through the proton–proton interactions and lattice distortions.¹²³ Besides, the proton environment was greatly affected by the dynamic motion of the oxygen atom.

Mazzei *et al.*¹²² also calculated the change in the hydrogen bond length with simulation times by calculating the vibrational density of states through *ab initio* molecular dynamics simulations. The length of hydrogen bond with $\nu(\text{O}-\text{H})$ mode fluctuated around 0.965–1.05 Å, while the length of hydrogen bond with $\delta(\text{O}-\text{H})$ mode and the lattice dynamics fluctuated around 1.84–2.22 Å (Fig. 4d).

Thus, the reorientation of the –OH group possibly occurred as the hydrogen bond became weak due to oxygen motion, while the proton hopping was enhanced as the hydrogen bond strengthened. Therefore, the trapped proton in BZI possibly did not hinder the proton conductivity, as it could move along with the movement of the oxygen atoms.

2.3. Extended X-ray absorption of fine structure

X-ray absorption spectroscopy (XAS) can provide information on the electronic and local structures of materials¹²⁴ and was shown to be sensitive to symmetry changes.¹²⁵ Giannici *et al.*^{126–128} studied the effect of protons on the crystal structure of $\text{BaCe}_{1-x}\text{M}_x\text{O}_{3-\delta}$ ($\text{M} = \text{In, Gd, and Y}$) by extended X-ray absorption fine structure (EXAFS), where the protons obviously affected the environments of Gd and Y and had no impact on those of In and Ce. Doping with Y or Gd resulted in minor modifications to the electronic and/or atomic structures of the host matrix, and

the negative charges around the dopant could effectively attract positively charged defects, providing a clear improvement of proton conductivity for BaCeO_3 when used in a smaller amount. On the contrary, the In element can be fully soluble and rearranges the electronic structure of BaCeO_3 , leading to lower proton conductivity. Han *et al.*¹²⁹ reported the effect of hydration on the pyrochlore oxide $\text{La}_2(\text{Nb}_{0.4}\text{Y}_{0.6})_2\text{O}_{7-\delta}$ (LNY) structure, as the basic unit of a tetrahedron consisting of two La atoms occupying the A sites, two Nb/Y atoms occupying the B sites and oxygen atoms in the centre, as shown in Fig. 5a. When

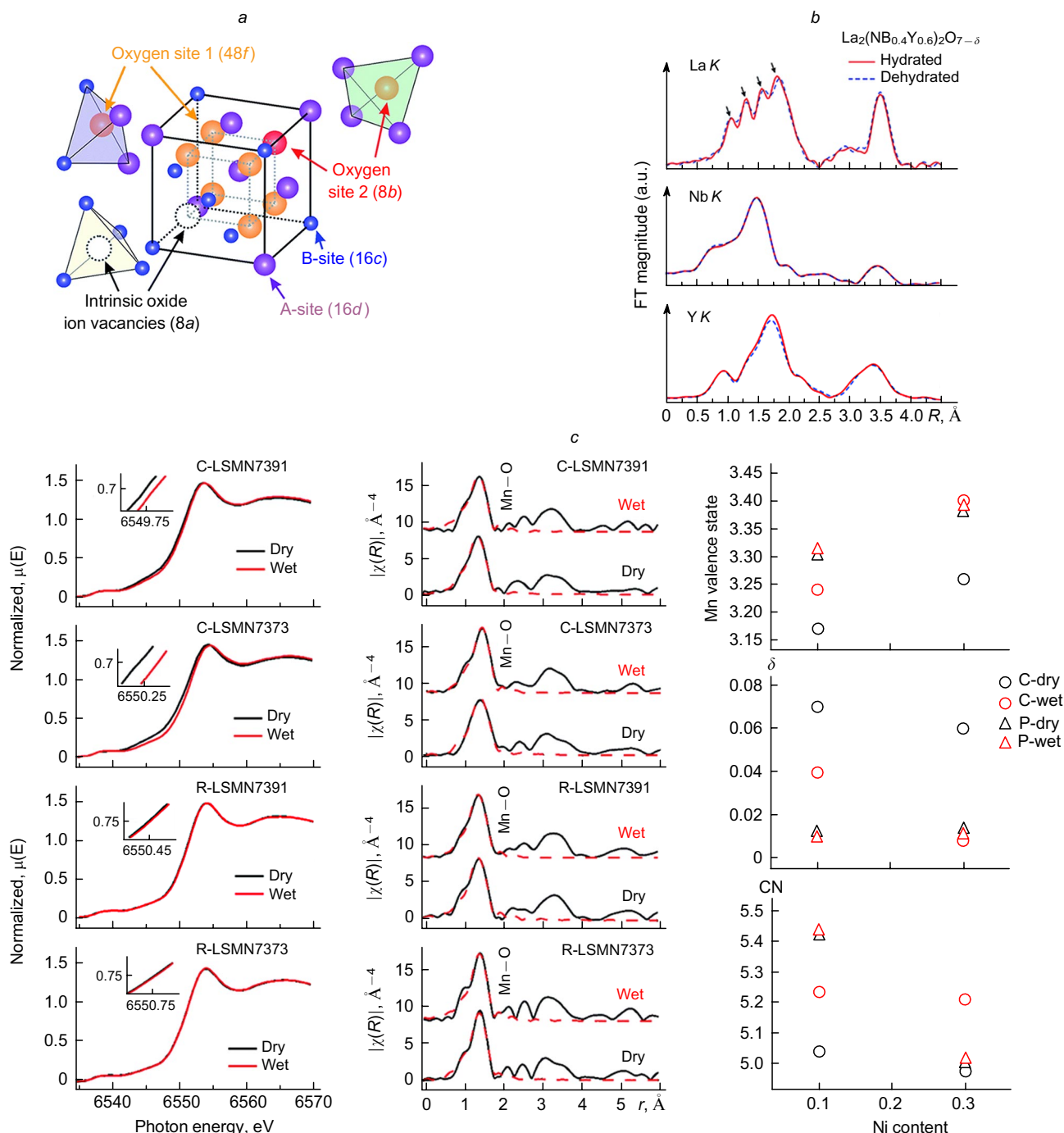


Figure 5. Reduced cubic pyrochlore structure (a). In $\text{La}_2(\text{Nb}_{1-x}\text{Y}_x)_2\text{O}_{7-\delta}$, La occupies A sites, and Nb and Y occupy B sites.¹²⁹ Fourier transform EXAFS spectra of hydrated and dehydrated $\text{La}_2(\text{Nb}_{0.4}\text{Y}_{0.6})_2\text{O}_{7-\delta}$ collected at the La K, Nb K and Y K-edges *in vacuo* at 10 K (b). Reproduced from Ref. 129 with permission from the Royal Society of Chemistry. *In situ* Mn K-edge XANES spectra (c). Reproduced from Ref. 130 with permission from the Royal Society of Chemistry.

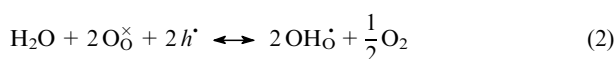
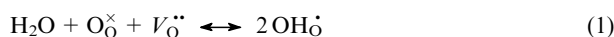
water was incorporated into LNY at 300 °C in 5% H₂O–95% Ar, the intensities of the Y K-edge and La K-edge were enhanced, while the intensity of the Nd K-edge remained almost unchanged (Fig. 5b), indicating that the oxygen sites around Y or La, but distal from Nd, participated in the hydration reaction. Wang *et al.*¹³⁰ used EXAFS to analyze the value changes of the Co and Mn elements in rhombohedral-type La_{0.7}Sr_{0.3}Mn_{1-x}Ni_xO_{3-δ} (r-LSMN) and cubic-type La_{0.7}Sr_{0.3}Mn_{1-x}Ni_{1-x}O_{3-δ} (c-LSMN) after hydration (Fig. 5c). The values of Ni ions in all LSMNs remained at +3, while the coordination numbers of Mn in c-LSMN7391 and c-LSMN7373 increased from 5.04 ± 0.55 and 4.98 ± 0.62 to 5.24 ± 5.21 ± 0.56, and those in r-LSMN7391 and r-LSMN7373 were almost unchanged. Therefore, the main hydration reaction occurred at the oxygen site around Mn and away from Ni in c-LSMN, indicating that c-LSCM presented the best proton uptake and conduction ability compared with r-LSCM, proved by the result of TGA and the single cell performance.

3. Determination of proton concentration

Although the spectrum method can provide information about the hydrogen bond type and the corresponding relative amount, the specific concentration cannot be obtained, making it difficult to directly compare the proton uptake ability with different materials. However, this problem can be easily resolved by TGA,^{83, 131–151} which makes it possible to measure the mass changes immediately at different water pressures and temperatures in experiments. Thus, the entropies (ΔH), enthalpies (ΔS) and Gibbs free energies (ΔG) of the proton uptake reaction were calculated, indicating the basic nature of the material. Furthermore, the Karl Fischer titration method^{28, 41, 152–157} and cold neutron prompt-gamma activation analysis (PGAA)^{103, 104} can also be used to analyze the absorbed proton concentrations at certain water pressure and temperature. In addition, the temperature programmed desorption of H₂O (H₂O-TPD) can provide the comparison of the adsorbed water amounts between different materials.

3.1. Thermogravimetric analysis

Protons can be absorbed under humid conditions by two reactions: the hydration reaction [Eq. (1)] and hydrogenation reaction [Eq. (2)]:⁴²



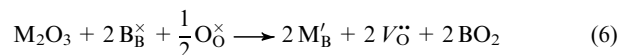
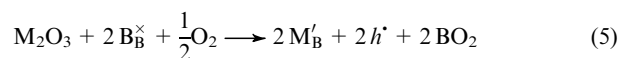
where the equilibrium constant (*K*) can be calculated by the following equations:

$$K_{\text{hydra}} = \frac{[\text{OH}_\text{O}^\bullet]^2}{p_{\text{H}_2\text{O}}[V_\text{O}^\bullet][\text{O}_\text{O}^\times]} = \exp\left(\frac{\Delta_{\text{hydra}}S}{R}\right) \exp\left(-\frac{\Delta_{\text{hydra}}H}{RT}\right) \quad (3)$$

$$K_{\text{hydro}} = \frac{p_{\text{O}_2}^{1/2}[\text{OH}_\text{O}^\bullet]^2}{p_{\text{H}_2\text{O}}[\text{O}_\text{O}^\times]^2[h^\bullet]^2} = \exp\left(\frac{\Delta_{\text{hydro}}S}{R}\right) \exp\left(-\frac{\Delta_{\text{hydro}}H}{RT}\right) \quad (4)$$

where [OH_O[•]], [V_O[•]], [O_O[×]] and [h[•]] denote the proton, oxygen vacancy, oxide ion at the normal oxygen site and the defect electron concentration of the material under wet conditions, respectively, and *p*_{H₂O} and *p*_{O₂} are the partial water pressure and oxygen pressure under test conditions, respectively. The hydration that occurred alone at [V_O[•]] was much high than

that at [h[•]], while hydrogenation proceeded alone under opposite conditions. For the acceptor doping material AB_{1-x}M_xO_{3-δ} (ABMO), the electron defect or oxygen vacancy can be generated by the reaction 5 or 6, respectively



Therefore, this will result in a defect equilibrium [Eq. (7)] and oxygen mass balance [Eq. (8)]:

$$[\text{M}'_\text{B}] = 2\text{M}'_\text{B} + 2h^\bullet + 2\text{BO}_2 \quad (7)$$

$$[\text{OH}_\text{O}^\bullet] + [V_\text{O}^\bullet] + [\text{O}_\text{O}^\times] = 3 \quad (8)$$

The defect concentration was governed by *p*_{H₂O} and *p*_{O₂}, where the electronic defect can be neglected at low temperatures.³² In addition, [OH_O[•]] can be calculated by Eq. (9):¹⁵⁸

$$[\text{OH}_\text{O}^\bullet] = 2 \frac{\Delta m}{m_0} \frac{M_{\text{ABM}}}{M_{\text{H}_2\text{O}}} \quad (9)$$

where *m*₀ is the mass of the dried sample, Δ*m* is the mass uptake after hydration, and *M*_{ABM} and *M*_{H₂O} are the molecular weights of ABM and H₂O, respectively.

The pretreatment of a sample was important for TGA experiments, since it is sensitive to minor weight variations, the specific surface area of sample should be low enough to avoid the effect of surface adsorption, and the adsorbed species on the sample should be washed out to a constant weight. The proton uptake results reported in the literature are summarized in Table 2. The effects of electron defects on BaZr_{0.8}Y_{0.2}O_{3-δ} at a temperature of 500 °C were observed,⁹² where Δ*H* was −26 ± 1 and −79.4 KJ mol^{−1} at 50–500 °C and 500–900 °C, respectively. Lim *et al.*¹³³ reported that Δ*H* and Δ*S* of proton uptake for BaCe_{0.9}Y_{0.1}O_{3-δ} in a temperature range of 1000–750 °C were −138.0 ± 6.9 and −142.2 ± 6.1, −147.8 ± 8.2 and −72.4 ± 7.2, and −144.7 ± 3.7 KJ mol^{−1} and −147.8 ± 3.2 J mol^{−1} K^{−1}, respectively, determined from the hydration reaction, hydrogenation reaction and a combination of two reactions simultaneously, indicating that the two proton uptake reactions occurred at the same time at high temperatures. Zohourian *et al.*¹⁵³ found that there was a positive linear correlation between Δ*G* of the hydration reaction and the average ‘ion electronegativity’ of the material, which can be defined by the ratio of the ion charge (*Z*) and the square of the radius (*r*), *Z*/*r*², based on the acid-base theory (Fig. 6a). However, their DFT results¹⁵⁹ further revealed the lower ionization potential of the ternary oxides with a perovskite structure due to the lower proton affinities with higher hydroxide ion affinities (Fig. 6b,c). Therefore, the proton uptake is affected by numerous intrinsic properties, not just the basicity.

Ren *et al.*¹³⁴ used the thermogravimetric relaxation technique and found that Ba deficiency was favourable for the reaction rate and the amount of proton uptake for BaCo_{0.4}Fe_{0.4}Zr_{0.1}Y_{0.1}O_{3-δ} (BCFZY). Figure 6d shows a good way to test the proton uptake rate of cathode materials for PCFCs. Huang *et al.*¹⁶⁰ found that NiO as a sintering aid could greatly decrease the proton concentration and value of *K*_{hydra} for a Ba_{1.015}Zr_{0.63}Ce_{0.20}Y_{0.17}O_{3-δ} pellet prepared by solid state reactive sintering approach (SSRS), which is much lower than that of a pellet prepared

Table 2. Results of hydration reported in the literature.

| Sample | $p_{\text{H}_2\text{O}}$, atm | $[\text{OH}^-]$, mol mol^{-1} | Temperature, $^{\circ}\text{C}$ | ΔH , kJ mol^{-1} | ΔS , $\text{J mol}^{-1} \text{K}^{-1}$ | Ref. |
|---|-----------------------------------|--|------------------------------------|---|--|------|
| BaCe _{0.9} Y _{0.1} O _{3-δ} | 0.024 | 0.003 | 600 | -50 ± 1 (250–800 $^{\circ}\text{C}$) | -88 ± 1 (250–800 $^{\circ}\text{C}$) | 131 |
| BaCe _{0.6} Zr _{0.3} Y _{0.1} O _{3-δ} | 0.024 | 0.008 | 600 | -66 ± 2 (250–800 $^{\circ}\text{C}$) | -118 ± 3 (250–800 $^{\circ}\text{C}$) | 131 |
| BaCe _{0.2} Zr _{0.7} Y _{0.1} O _{3-δ} | 0.024 | 0.015 | 600 | -84 ± 3 (250–800 $^{\circ}\text{C}$) | -122 ± 5 (250–800 $^{\circ}\text{C}$) | 131 |
| BaCe _{0.1} Zr _{0.9} Y _{0.1} O _{3-δ} | 0.024 | 0.023 | 600 | -68 ± 2 (250–800 $^{\circ}\text{C}$) | -108 ± 2 (250–800 $^{\circ}\text{C}$) | 131 |
| BaCe _{0.9} Y _{0.1} O _{3-δ} | ~ 0.0025 | ~ 0.05 | 300 | NM | NM | 83 |
| BaCe _{0.90} Y _{0.10} O _{3-δ} | 1 | ~ 0.01 | 300 | NM | NM | 132 |
| BaCe _{0.9} Y _{0.1} O _{3-δ} | 0.0063 | 0.045 | 400 | -144.7 ± 3.7 (750–1000 $^{\circ}\text{C}$) | NM | 133 |
| Ba _{0.95} Co _{0.4} Fe _{0.4} Zr _{0.1} Y _{0.1} O _{3-δ} | 0.1 | 0.0232 | 500 | NM | NM | 134 |
| BaCo _{0.4} Fe _{0.4} Zr _{0.1} Y _{0.1} O _{3-δ} | 0.1 | 0.0174 | 500 | NM | NM | 134 |
| BaCo _{0.4} Fe _{0.4} Zr _{0.1} Y _{0.1} O _{3-δ} | 0.0095 | 1.9% | 500 | NM | NM | 135 |
| Ba _{0.95} Ag _{0.05} Co _{0.4} Fe _{0.4} Zr _{0.1} Y _{0.1} O _{3-δ} | 0.01 | NM | NM | NM | NM | 135 |
| BaGd _{0.8} La _{0.2} Co ₂ O _{6.75} | 0.02 | 0.03 | 400 | -50 ± 7 | -140 ± 10 | 136 |
| BaNd _{0.8} Ca _{0.2} InO _{3.9} | 0.03 | 0.022 | 500 | NM | NM | 137 |
| BaSn _{0.95} Y _{0.05} O _{3-δ} | 0.024 | ~ 0.032 | 600 | -46 ± 3 (250–800 $^{\circ}\text{C}$) | -95 ± 5 (250–800 $^{\circ}\text{C}$) | 138 |
| BaSn _{0.875} Y _{0.125} O _{3-δ} | 0.024 | 0.003 | 600 | -50 ± 1 (250–800 $^{\circ}\text{C}$) | -88 ± 1 (250–800 $^{\circ}\text{C}$) | 138 |
| BaSn _{0.75} Y _{0.25} O _{3-δ} | 0.024 | 0.008 | 600 | -66 ± 2 (250–800 $^{\circ}\text{C}$) | -118 ± 3 (250–800 $^{\circ}\text{C}$) | 138 |
| BaSn _{0.625} Y _{0.375} O _{3-δ} | 0.024 | 0.015 | 600 | -84 ± 3 (250–800 $^{\circ}\text{C}$) | -122 ± 5 (250–800 $^{\circ}\text{C}$) | 138 |
| BaSn _{0.5} Y _{0.5} O _{3-δ} | 0.024 | 0.023 | 600 | -68 ± 2 (250–800 $^{\circ}\text{C}$) | -108 ± 2 (250–800 $^{\circ}\text{C}$) | 138 |
| Ba _{0.8} Sr _{0.2} Ti _{0.9} Fe _{0.1} O _{3-δ} | ~ 0.02 | ~ 0.05 | 300 | NM | NM | 139 |
| Ba _{0.5} Sr _{0.5} Ti _{0.9} Fe _{0.1} O _{3-δ} | ~ 0.02 | ~ 0.01 | 300 | NM | NM | 139 |
| BaTi _{0.8} Sc _{0.2} O _{2.9} | 1 | ~ 0.08 | 400 | -83 ± 2 (500 $^{\circ}\text{C}$) | -92 ± 2 (500 $^{\circ}\text{C}$) | 140 |
| BaTi _{0.5} Sc _{0.5} O _{2.75} | 1 | ~ 0.03 | 400 | -779 ± 2 (500 $^{\circ}\text{C}$) | -136 ± 2 (500 $^{\circ}\text{C}$) | 140 |
| BaTi _{0.4} Sc _{0.6} O _{2.7} | 1 | 0.09 | 400 | -57 ± 4 (500 $^{\circ}\text{C}$) | -127 ± 4 (500 $^{\circ}\text{C}$) | 140 |
| BaTi _{0.3} Sc _{0.7} O _{2.65} | 1 | ~ 0.16 | 400 | -108 ± 2 (500 $^{\circ}\text{C}$) | -146 ± 2 (500 $^{\circ}\text{C}$) | 140 |
| BaTi _{0.3} In _{0.7} O _{2.65} | 1 | ~ 0.10 | 400 | -73 ± 2 (500 $^{\circ}\text{C}$) | -127 ± 2 (500 $^{\circ}\text{C}$) | 140 |
| BaTi _{0.5} In _{0.5} O _{2.65} | 1 | ~ 0.035 | 400 | -53 ± 5 (500 $^{\circ}\text{C}$) | -126 ± 5 (500 $^{\circ}\text{C}$) | 140 |
| BaZr _{0.75} In _{0.25} Bi _{0.05} O _{3-δ} | 0.281 | 0.032 | 500 | -56 | -34 | 141 |
| BaZr _{0.9} Pr _{0.1} O ₃ | 0.015 | NM | NM | -43.14 (400 $^{\circ}\text{C}$) | NM | 22 |
| BaZr _{0.5} Pr _{0.5} O ₃ | 0.015 | NM | NM | -44.27 (400 $^{\circ}\text{C}$) | NM | 22 |
| BaZr _{0.8} Sc _{0.2} O _{3-δ} | 0.2 | 0.17 | 200 | NM | NM | 142 |
| BaZr _{0.7} Sn _{0.1} Sc _{0.2} O _{3-δ} | 0.2 | 0.175 | 200 | NM | NM | 142 |
| BaZr _{0.90} Gd _{0.10} O _{3-δ} | 1 | 0.09 | 250 | -66.1 (600–900 $^{\circ}\text{C}$) | -85.9 (600–900 $^{\circ}\text{C}$) | 92 |
| BaZr _{0.90} In _{0.10} O _{3-δ} | 1 | 0.06 | 250 | -66.6 (450–900 $^{\circ}\text{C}$) | -90.2 (450–900 $^{\circ}\text{C}$) | 92 |
| BaZr _{0.98} Y _{0.02} O _{3-δ} | 1 | 0.017 | 250 | -80.9 (500–900 $^{\circ}\text{C}$) | -99.4 (500–900 $^{\circ}\text{C}$) | 92 |
| BaZr _{0.90} Y _{0.10} O _{3-δ} | 1 | 0.10 | 250 | -79.4 (500–900 $^{\circ}\text{C}$) | -88.8 (500–900 $^{\circ}\text{C}$) | 92 |
| BaZr _{0.80} Y _{0.20} O _{3-δ} | 1 | 0.18 | 250 | -93.3 (550–900 $^{\circ}\text{C}$) | -103.2 (550–900 $^{\circ}\text{C}$) | 92 |
| BaZr _{0.90} Y _{0.10} O _{3-δ} | 0.1–1.0 | NM | NM | -81 ± 4 (300–900 $^{\circ}\text{C}$) | NM | 132 |
| (Ca _{0.87} Ni _{0.03})Ti ₁ O _{2.80} (OH) _{0.20} | NM | 0.183 | NM | NM | NM | 100 |
| La _{0.8} Sr _{0.2} Co _{0.8} Ni _{0.2} O _{3-δ} | 0.023 | 0.082 | 405 | NM | NM | 143 |
| La _{0.8} Sr _{0.2} Co _{0.7} Ni _{0.3} O _{3-δ} | 0.023 | 0.062 | 405 | NM | NM | 143 |
| La _{0.8} Sr _{0.2} Co _{0.7} Ni _{0.3} O _{3-δ} | 0.023 | 0.025 | 500 | NM | NM | 143 |
| La _{0.8} Sr _{0.2} Co _{0.7} Ni _{0.3} O _{3-δ} | 0.023 | 0.0022 | 600 | NM | NM | 143 |
| SrCe _{0.977} Yb _{0.023} O _{3-δ} | 1 | NM | 900 | -157 (500–900 $^{\circ}\text{C}$) | -128 (500–900 $^{\circ}\text{C}$) | 144 |
| SrTi _{0.9} Fe _{0.1} O _{3-δ} | 0.02 | ~ 0.085 | 300 | NM | NM | 139 |
| SrZr _{0.5} Co _{0.4} Y _{0.1} O _{3-δ} | 0.019 | 0.095 | 100 | -62.56 (600–1200) | -70.1 (600–1200) | 145 |
| Ba ₃ Co ₂ O ₆ (CO ₃) _{0.6} | 0.03 | NM | 400 | NM | NM | 146 |
| Ba ₂ YSnO _{5.5} | 0.016 | 1 | 250 | -89.1 (200–700 $^{\circ}\text{C}$) | -73.7 (200–700 $^{\circ}\text{C}$) | 85 |
| PrBa _{0.8} Ca _{0.2} Co ₂ O _{5+δ} | 0.03 | NM | 500 | $-NM$ | NM | 147 |
| PrBa _{0.5} Sr _{0.5} Co _{1.5} Fe _{0.5} O _{5+δ} | 0.02 | 0.017 | 600 | -22 (400 $^{\circ}\text{C}$) | -63 (400 $^{\circ}\text{C}$) | 148 |
| Sr ₂ Fe _{1.5} Mo _{0.4} Zr _{0.1} O _{6-δ} | 0.02 | 0.48 | 400 | NM | NM | 149 |
| Sr ₂ Fe _{1.5} Mo _{0.5} O _{6-δ} | 0.02 | NM | NM | NM | NM | 149 |
| BaLaInO ₄ | NM | 0.62 | NM | NM | NM | 150 |
| Ba _{1.1} La _{0.9} InO _{3.95} | NM | 1.05 | NM | NM | NM | 150 |
| Ba _{1.1} La _{0.9} Y _{0.5} In _{0.5} O _{3.95} | NM | 1.90 | NM | NM | NM | 150 |
| La ₃ NbO ₇ | 0.023 | ~ 0.001 | 600 | NM | NM | 151 |
| Ga ₃ NbO ₇ | 0.023 | ~ 0.012 | NM | NM | NM | 151 |
| Ga ₃ NbO ₇ | 0.023 | ~ 0.018 | NM | NM | NM | 151 |
| Yb ₃ NbO ₇ | 0.023 | ~ 0.019 | NM | NM | NM | 151 |
| Y ₃ NbO ₇ | 0.023 | ~ 0.026 | NM | NM | NM | 151 |
| Ba ₃ Ca _{1.17} Nd _{1.83} O _{9-δ} | 0.023 | 0.495 | 250 | -68.7 (200–700 $^{\circ}\text{C}$) | -108.1 (200–700 $^{\circ}\text{C}$) | 85 |

Note. NM is not measured.

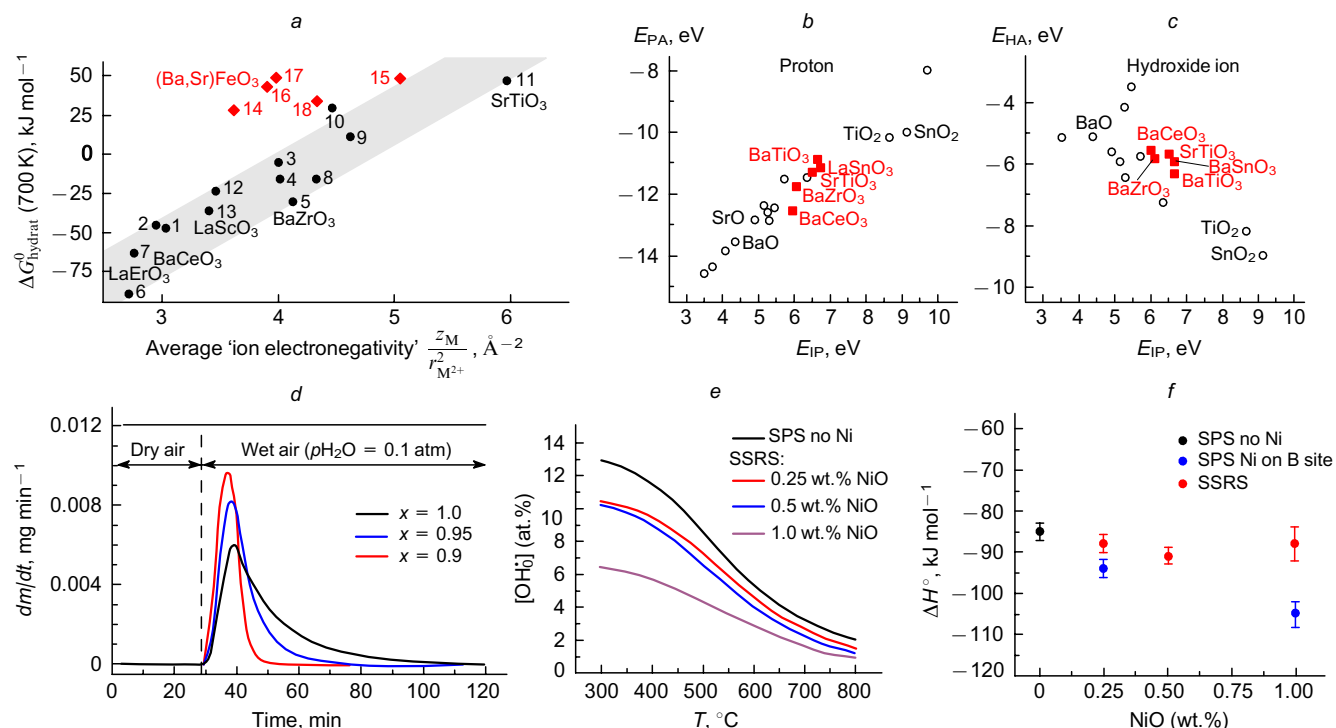


Figure 6. Standard Gibbs energy of the hydration reaction (ΔG_{hydrat}) at 700 K plotted vs. the average ion electronegativity (a). Reproduced from Ref. 153 with permission from Elsevier. The calculated proton (b) and hydroxide ion affinities (c) as a function of the calculated ionization potential of BaXO₃ (X = Ti, Sn, Zr, and Ce), SrTiO₃ perovskites (BO₂ termination) and the binary oxides. Reproduced from Ref. 159 with permission from the American Chemical Society. Thermogravimetric relaxation curves of the B_xCFZY oxides (d). Reproduced from Ref. 134 with permission from the Royal Society of Chemistry. Proton uptake (e) and standard hydration enthalpy (f) of Ba_{1.015}Zr_{0.664}Ce_{0.20}Y_{0.136}O_{3-δ} with different NiO content. Reproduced from Ref. 134 with permission from the Royal Society of Chemistry.

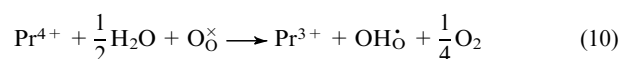
by spark plasma sintering (SPS) without NiO (Fig. 6e,f). With the use of NiO, the effective acceptor concentration with the formation of $[\text{Y}_{\text{Ba}}]$ defects at the A site in the crystal decreased and that of the impurity phases increased, and even positively charged $[\text{Ni}_{\text{Zr}}^{\bullet}]$ defects at the B site can trap the protons to decrease the entropy and enthalpy. Therefore, the free-NiO aid was suggested as an addition to electrolytes during the preparation of full cells for NiO diffusion from the anode to the electrolyte.^{23,161,162}

3.2. Methods of H₂O-TPD, PGAA and Karl Fischer titration

The temperature programmed desorption of H₂O was carried out by monitoring the H₂O signals at elevated temperatures from a saturated sample using a mass spectrometer.^{78,163–166} The temperature of the peak centre illustrated the desorption temperature and the area can represent the amounts of desorbed water. Wang *et al.*^{165,166} found that the water adsorption rates of Ni–BaZrO₃, Ni–BaZr_{0.1}Ce_{0.7}Y_{0.2}O₃, Ni–BaZr_{0.4}Ce_{0.4}Y_{0.2}O₃ and Ni–BaZr_{0.1}Ce_{0.7}Y_{0.1}Yb_{0.1}O_{3-δ} were 2.91×10^{-5} , 5.7×10^{-5} , 1.19×10^{-4} and $1.12 \times 10^{-4} \text{ mol g}^{-1} \text{ min}^{-1}$, respectively. Therefore, Ni–BaZr_{0.4}Ce_{0.4}Y_{0.2}O₃ and Ni–BaZr_{0.1}Ce_{0.7}Y_{0.1}Yb_{0.1}O_{3-δ} were better anode materials for PCFC. Furthermore, the B-site cation deficiency can further enhance the hydration ability of BaZr_{0.1}Ce_{0.7}Y_{0.1}Yb_{0.1}O_{3-δ}.¹⁶⁴ Zhou *et al.*¹⁶³ proved that Ba₂Sc_{0.1}Nb_{0.1}Co_{1.5}Fe_{0.3}O_{6-δ} (BSNCF) was much more suitable than Sr₂Sc_{0.1}Nb_{0.1}Co_{1.5}Fe_{0.3}O_{6-δ} (SSNCF) as a cathode material for PCFC by H₂O-TPD, since BSNCF had a stronger adsorption capacity for a higher desorption

temperature and a better hydration ability for a larger peak area than SSNCF (Fig. 7a).

When induced by a neutrons beam, using the PGAA, it is possible to collect the gamma rays of elements, where the intensity of the signal is proportional to the element concentration.¹⁶⁷ Jones *et al.*¹⁰³ found that the Pr⁴⁺ site participated in proton uptake described by the following equation:



The PGAA results showed that the H : Y mole ratio was 5 in protonated BaPr_{1-x}Y_xO₃ (BPY) at 400–500 °C under 3% water for a few hours, which was much higher than the theoretical value calculated from the concentration of oxygen vacancies with Y doping (Fig. 7b). The reduction of Pr⁴⁺ to Pr³⁺ in BPY after proton uptake was confirmed by X-ray photoelectron spectroscopy (XPS) (Fig. 7c). Furthermore, the H : Y mole ratio in protonated BaCe_{0.9}Y_{0.1}O₃ was 0.87, which is similar to other reported values and confirmed the reliability of the PGAA results.

The scheme of the Karl–Fischer titration test method is shown in Fig. 7d.¹⁵² The sample was saturated at a certain temperature and water pressure. Then the protonated sample was heated at a high temperature and the vapour was transported by a dry carrier gas to the titration device, which was used to test the adsorbed water content.

Han *et al.*¹⁵² found that Fe doping can obviously decrease the proton concentration of La_{1-x}Sr_xSc_{1-y}Fe_yO_{3-δ}, the Sr doping is benefit to the

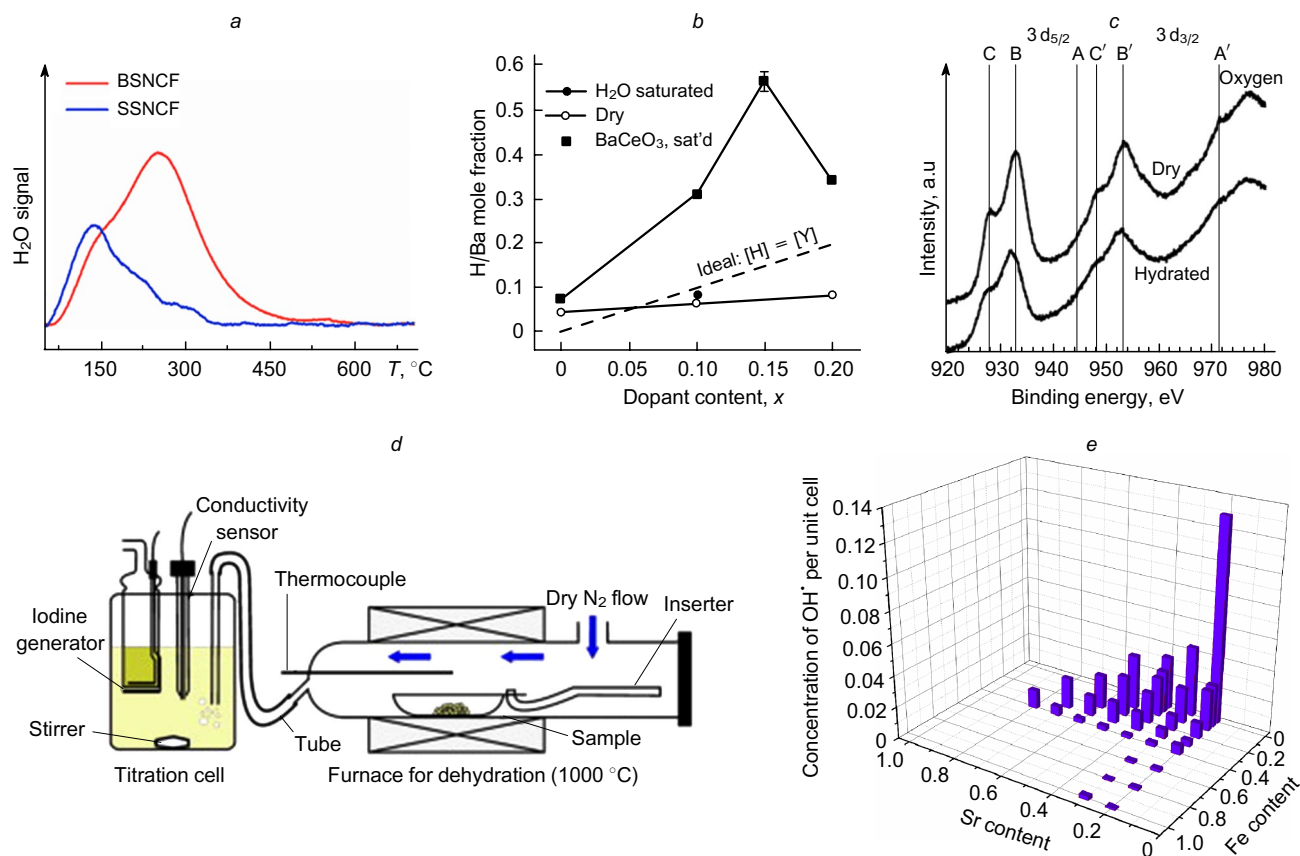


Figure 7. H₂O-TPD of BSNCF and SSNCF electrodes treated under 20 vol.% H₂O for 2 h at 550 °C and then quenched to room temperature (a). Reproduced from Ref. 163 with permission from Elsevier. Hydrogen concentration in saturated and dry BaPr_{1-x}Y_xO_{3-δ} as measured by PGAA and comparison with saturated BaCe_{0.8}Y_{0.2}O_{3-δ} (b).¹⁰³ Comparison of the X-ray photoemission spectra obtained from BaPrO₃ in the dry and hydrated states (c). Reproduced from Ref. 103 with permission from AIP Publishing. Schematic of a Karl-Fischer moisture titrator for determining the water content of the samples (d).¹⁵² Three-dimensional plots of the concentration of hydroxide ions per unit cell of LSSF (e). La_{1-x}Sr_xSc_{1-y}Fe_yO_{3-δ}, hydration conditions: $p_{\text{H}_2\text{O}}$ 0.05 atm, p_{O_2} 0.19 atm, p_{Ar} 0.76 atm, 300 °C, 48 h. Dehydration conditions: 1000 °C, dry N₂. The measured samples were of the size about 2 mm in length, broken from pellets sintered at 1500 °C. Reproduced from Ref. 152 with permission from Elsevier.

proton uptake as $y \geq 0.2$ and plays an opposite role as $y = 0$. Besides, the change trend of proton concentration is similar to that of the oxygen vacancy concentration in La_{1-x}Sr_xSc_{1-y}Fe_yO_{3-δ} (Fig. 7e). Protonated La_{0.8}Sr_{0.2}ScO_{3-δ} had the highest proton concentration of 0.13 mol unit⁻¹. Han *et al.*¹⁵⁵ also reported that the proton concentration of protonated BaZr_{1-x}Y_xO_{3-δ} under 5% H₂O-Ar at 300 °C increased from around 0.024 with $x = 0.05$ to 0.19 with $x = 0.3$ following the Karl-Fischer titration, and the dehydration phenomenon was observed as the proton concentration of the sample decreased at higher hydration temperatures.

4. Conclusion

In this review, we summarized different methods for detecting the proton concentration and distribution in the crystal structure. Hydrogen bonding vibrations can be represented by two models, bending and stretching, which often occur under coupling with the total wavenumber located in the range of 4100–4300 cm⁻¹. The protons in the crystal were not only in the form of hydrogen bonds but also in the form of ionic protons, polaronic protons with extremely low vibrational frequencies and paired protons with higher vibrational frequencies compared with hydrogen bonds.

The proton can be located both in symmetric and asymmetric environments. The hydrogen bonds in the former environment are weak, own higher vibrational frequency and act as valid mobile carries, while the hydrogen bonds in the latter environment are stronger and hardly to be broken with lower vibrational frequency. Therefore, the proton is easily transferred among neighbouring oxygens and the reorientation of the proton is difficult, resulting in the lower proton conductivity. Besides, the protons can also be trapped in the grain boundaries, leading to stronger hydrogen bonds and a decrease in the proton conductivity in most cases. A high proton concentration may be achieved with minor modification of the doping elements in the electronic and/or atomic structure of the host material.

Compared with the Raman spectrum, inelastic neutron scattering and X-ray absorption spectroscopy, the IR spectrum is the most direct, common, simplest and sensitive way to detect the hydroxyl signal with stretching mode in the material. Therefore, the IR spectrum can directly present the change in hydrogen bonding. The Raman spectrum relates to the vibration of the host lattice and it can be used to analyze the interaction between the proton and host lattice. Both IR and Raman methods can realize the in-suit collection of a hydroxyl signal at various temperatures, which is suitable to acquire the vibrational and diffusional

dynamics. The surface proton species should be avoided in the test of bulk proton for the vibration signal or proton concentration. The specific surface area of the test sample should be lower enough to decrease the adsorption of impurity. Besides, polishing the sample and thermal treating at high temperature could wipe out the unstable species before the test. The detection of an isotope, such as deuterium and O^{18} , is another effective way to distinguish between the surface and bulk species.

The study of proton distribution by the wave spectroscopy is most applied to electrolyte materials, while the main work on oxygen electrode materials is to detect the proton concentration with TGA and the proton conductivity with the four-probe method. There are few reports about the proton distribution to establish the relationship between the structure and the proton transport in current research. The crystal structure of an electrode material also contains lots of distortion from the element doping and ionic defects, so the proton can be trapped in some strong hydrogen bonds. Therefore, the high proton concentration may lead to low proton conductivity, which is the object of further investigations. Moreover, the basic property of materials is studied using them as powders and pellets under certain condition, while the actual environment in cell is much more complex at varied water pressure, oxygen pressure, voltage, current and temperature. Therefore, the test of in-suit cell is necessary to obtain the actual proton distribution and transport behaviour under the working condition.

This research was financially supported by the National Key Research & Development Program of China (2018YFE0124700), the National Natural Science Foundation of China (52072134, U1910209, 51972128) and Hubei Province (2021CBA149, 2021CFA072, 2022BAA087).

5. List of acronyms and designations

ABMO — $AB_{1-x}M_xO_{3-\delta}$ perovskite,
 AC — asymmetric configuration,
 BCFZY — $BaCo_{0.4}Fe_{0.4}Zr_{0.1}Y_{0.1}O_{3-\delta}$,
 BCN-18 — $Ba_3(Ca_{1.18}Nb_{1.82})O_{9-\delta}$,
 BCO — $BaCeO_3$,
 BCY91 — $BaCe_{0.9}Y_{0.1}O_{2.95}$,
 BIO — $Ba_2In_2O_5$,
 BPY — $BaPr_{1-x}Y_xO_3$,
 BSNCf — $Ba_2Sc_{0.1}Nb_{0.1}Co_{1.5}Zr_{0.4}Fe_{0.3}O_{6-\delta}$,
 BZCY442 — $BaCe_{0.4}Zr_{0.4}Y_{0.2}O_{3-\delta}$,
 BZCYyb — $BaZr_{0.1}Ce_{0.7}Y_{0.1}Yb_{0.1}O_{3-\delta}$,
 BZI — $BaZr_{1-x}In_xO_{3-x/2}$, $BaZr_{1-x}In_xO_{3-\delta}$,
 BZN — $Ba(Zn_{0.4}Nb_{0.6})O_{3-\delta}$,
 BZY — $BaZr_{1-x}Y_xO_3$,
 BZY91 — $BaZr_{0.1}Y_{0.1}O_{2.95}$,
 BZYb91 — $BaZr_{0.9}Yb_{0.1}O_{3-\delta}$,
 EDX — energy-dispersive X-ray spectroscopy,
 EXAFS — extended X-ray absorption fine structure,
 H₂O-TPD — temperature programmed desorption of H₂O,
 IR — infrared absorption,
 INS — inelastic neutron scattering,
 LNY — $La_2(Nb_{0.4}Y_{0.6})_2O_{7-\delta}$,
 c-LSMN — cubic-type $La_{0.7}Sr_{0.3}Mn_{1-x}Ni_{1-x}O_{3-\delta}$,
 c-LSMN7373 — cubic-type $La_{0.7}Sr_{0.3}Mn_{0.7}Ni_{0.3}O_{3-\delta}$,
 c-LSMN7391 — cubic-type $La_{0.7}Sr_{0.3}Mn_{0.9}Ni_{0.1}O_{3-\delta}$,
 r-LSMN — rhombohedral-type
 $La_{0.7}Sr_{0.3}Mn_{1-x}Ni_xO_{3-\delta}$,

r-LSMN7373 — rhombohedral-type
 $La_{0.7}Sr_{0.3}Mn_{0.7}Ni_{0.3}O_{3-\delta}$,
 r-LSMN7391 — rhombohedral-type
 $La_{0.7}Sr_{0.3}Mn_{0.9}Ni_{0.1}O_{3-\delta}$,
 ND — neutron diffraction,
 O-SOFC — oxygen ion-conducting SOFC,
 PCFC — protonic ceramic fuel cell,
 PGAA — prompt-gamma activation analysis,
 QENS — quasi-elastic neutron scattering,
 SBTAl — $Sr_{0.5}Ba_{0.5}Ti_{1-x}Al_xO_{3-\delta}$,
 SC — symmetric configuration,
 SOFC — solid oxide fuel cell,
 SPS — spark plasma sintering,
 SSNC — $SrSc_{0.175}Nb_{0.025}Co_{0.8}O_{3-\delta}$,
 SSNCf — $Sr_2Sc_{0.1}Nb_{0.1}Co_{1.5}Fe_{0.3}O_{6-\delta}$,
 SSRS — solid state reactive sintering approach,
 SZE — $SrZr_{0.95}Er_{0.05}O_{3-\delta}$,
 SZL91 — $SrZr_{0.9}Ln_{0.1}O_{3-\delta}$,
 SZY91 — $SrZr_{0.9}Y_{0.1}O_3$,
 SZY93 — $SrZr_{0.93}Y_{0.07}O_{3-\delta}$,
 SZYb91 — $SrZr_{0.9}Yb_{0.1}O_{3-\delta}$,
 TGA — thermogravimetric analysis,
 XAS — X-ray absorption spectroscopy,
 XPS — X-ray photoelectron spectroscopy.

6. References

- P.De Luna, C.Hahn, D.Higgins, S.A.Jaffer, T.F.Jaramillo, E.H.Sargent. *Science*, **364**, 3506 (2019)
- G.Weng, K.Ouyang, X.Lin, J.Xue, H.Wang. *React. Chem. Eng.*, **6**, 1739 (2021)
- D.Y.Voropaeva, S.A.Novikova, A.B.Yaroslavtsev. *Russ. Chem. Rev.*, **89**, 1132 (2020)
- J.Chen, J.Li, L.Jia, I.Moussa, B.Chi, J.Pu, J.Li. *J. Power Sources*, **428**, 13 (2019)
- S.P.Filippov, A.B.Yaroslavtsev. *Russ. Chem. Rev.*, **90**, 627 (2021)
- D.Xiong, S.A.Rasaki, Y.Li, L.Fan, C.Liu, Z.Chen. *J. Adv. Ceram.*, **11**, 40145 (2022)
- X.-B.Xie, Q.Xu, J.Xiao, M.Chen, D.-C.Chen, D.-P.Huang, F.Zhang. *Mater. Res. Bull.*, **131**, 110967 (2020)
- D.Xie, K.Li, J.Yang, D.Yan, L.C.Jia, B.Chi, J.Pu, J.Li. *Int. J. Hydrog. Energy*, **46**, 10007 (2020)
- E.Y.Pikalova, E.G.Kalinina. *Russ. Chem. Rev.*, **90**, 703 (2021)
- I.A.Zvonareva, A.M.Mineev, N.A.Tarasova, X.-Z.Fu, D.A.Medvedev. *J. Adv. Ceram.*, **11**, 1131 (2022)
- B.Liu, J.Yang, D.Yan, L.Jia, B.Chi, J.Pu, J.Li. *Int. J. Hydrog. Energy*, **45**, 31009 (2020)
- Y.Xu, X.Xu, L.Bi. *J. Adv. Ceram.*, **11**, 794 (2022)
- B.Liu, L.C.Jia, B.Chi, J.Pu, J.Li. *Compos. Part B Eng.*, **191**, 107936 (2020)
- X.Yang, X.Xu, S.Wu, S.Yu, L.Bi. *Ceram. Int.*, **48**, 19626 (2022)
- S.Y.Istomin, N.V.Lyskov, G.N.Mazo, E.V.Antipov. *Russ. Chem. Rev.*, **90**, 644 (2021)
- B.Liu, Z.Li, X.Yang, D.Yan, J.Li, L.Jia. *J. Mater. Chem. A*, **10**, 17425 (2022)
- X.Xu, Y.Xu, J.Ma, Y.Yin, M.Fronzi, X.Wang, L.Bi. *J. Power Sources*, **489**, 229486 (2021)
- X.Xu, H.Q.Wang, J.M.Ma, W.Y.Liu, X.F.Wang, M.Fronzi, L.Bi. *J. Mater. Chem. A*, **7**, 18792 (2019)
- L.Lin, Q.Xu, Y.-P.Wang, M.Chen, J.Xiao, D.-P.Huang, F.Zhang. *Mater. Res. Bull.*, **106**, 263 (2018)
- A.Subramanian, J.Tong, R.P.O'Hayre, N.M.Sammes. *J. Am. Ceram. Soc.*, **94**, 1800 (2011)
- A.Magrez. *Solid State Ion.*, **175**, 585 (2004)
- D.S.Tsvetkov, A.L.Sednev-Lugovets, D.A.Malyshkin, V.V.Sereda, A.Y.Zuev, I.L.Ivanov. *J. Phys. Chem. Solids*, **147** (2020)

23. H.Shimada, T.Yamaguchi, H.Sumii, Y.Yamaguchi, K.Nomura, Y.Fujishiro. *Ceram. Int.*, **44**, 3134 (2018)
24. M.Chen, X.Xie, J.Guo, D.Chen, Q.Xu. *J. Mater. Chem. A*, **8**, 12566 (2020)
25. T.Wei, P.Qiu, L.C.Jia, Y.Tan, X.Yang, S.C.Sun, F.L.Chen, J.Li. *J. Mater. Chem. A*, **8**, 9806 (2020)
26. N.N.M.Tahir, N.A.Baharuddin, A.A.Samat, N.Osman, M.R.Somalu. *J. Alloys Compd.*, **894**, 162458 (2022)
27. Y.Lin, R.Ran, C.M.Zhang, R.Cai, Z.P.Shao. *J. Phys. Chem. A*, **114**, 3764 (2010)
28. X.Xu, H.Q.Wang, M.Fronzi, X.F.Wang, L.Bi, E.Traversa. *J. Mater. Chem. A*, **7**, 20624 (2019)
29. L.Zhang, Y.Yin, Y.Xu, S.Yu, L.Bi. *Sci. China Mater.*, **65**, 1485 (2022)
30. J.Li, C.Wang, X.F.Wang, L.Bi. *Electrochem. Commun.*, **112**, v (2020)
31. M.A.Nur Syafkeena, M.L.Zainor, O. H.Hassan, N.A.Baharuddin, M.H.D.Othman, C.-J.Tseng, N.Osman. *J. Alloys Compd.*, **918**, 165434 (2022)
32. I.Zvonareva, X.-Z.Fu, D.Medvedev, Z.Shao. *Energy Environ. Sci.*, **15**, 439 (2021)
33. D.Neagu, G.Tsekouras, D.N.Miller, H.Menard, J.T.S.Irvine. *Nat. Chem.*, **5**, 916 (2013)
34. M.Z.Ahmad, S.H.Ahmad, R.S.Chen, A.F.Ismail, R.Hazan, N.A.Baharuddin. *Int. J. Hydrog. Energy*, **47**, 1103 (2022)
35. L.Mazzei, F.Piccinelli, M.Bettinelli, S.F.Parker, M.Karlsson. *Solid State Ion.*, **365**, 115624 (2021)
36. C.A.Fuller, Q.Berrod, B.Frick, M.R.Johnson, M.Avdeev, J.S.O.Evans, I.R.Evans. *Chem. Mater.*, **32**, 4347 (2020)
37. X.Chen, N.Hatada, K.Toyoura, T.Uda. *J. Am. Ceram. Soc.*, **105**, 6652 (2022)
38. J.E.F.S.Rodrigues, R.C.Costa, P.S.Pizani, A.C.Hernandes, J.A.Alonso. *J. Raman Spectrosc.*, **53**, 1333 (2022)
39. Y.Sakuda, J.R.Hester, M.Yashima. *J. Ceram. Soc. Jpn.*, **130**, 442 (2022)
40. R.Zohourian, R.Merkle, G.Raimondi, J.Maier. *Adv. Funct. Mater.*, **28**, 1801241 (2018)
41. D.Poetzsch, R.Merkle, J.Maier. *Faraday Discuss*, **182**, 129 (2015)
42. M.Papac, V.Stevanovic, A.Zakutayev, R.O'Hayre. *Nat. Mater.*, **20**, 301 (2020)
43. E.Fabbri, D.Pergolesi, S.Licoccia, E.Traversa. *Solid State Ion.*, **181**, 1043 (2010)
44. K.D.Kreuer. *Solid State Ion.*, **125**, 285 (1999)
45. R.Hempelmann, M.Soetratmo, O.Hartmann, R.Wäppling. *Solid State Ion.*, **107**, 269 (1998)
46. J.Cao, Y.Ji, Z.Shao. *Energy Environ. Sci.*, **15**, 2200 (2022)
47. M.Shahid. *Ionics*, **28**, 3583 (2022)
48. M.Coduri, M.Karlsson, L.Malavasi. *J. Mater. Chem. A*, **10**, 5082 (2022)
49. Y.Huang, R.Qiu, W.Lian, L.Lei, T.Liu, J.Zhang, Y.Wang, J.Liu, J.Huang, F.Chen. *J. Power Sources*, **528**, 231201 (2022)
50. D.Vignesh, B.K.Sonu, E.Rout. *Energy Fuels*, **36**, 7219 (2022)
51. M.N.Iliev, M.V.Abrashev. *J. Raman Spectrosc.*, **32**, 805 (2001)
52. B.-Z.Magnes, D.Pines, N.Strashnikova, E.Pines. *Solid State Ion.*, **168**, 225 (2004)
53. S.A.Prosandeev, U.Waghmare, I.Levin, J.Maslar. *Phys. Rev. B*, **71**, 214307 (2005)
54. M.N.Iliev, M.V.Abrashev, J.Laverdière, S.Jandl, M.M.Gospodinov, Y.-Q.Wang, Y.-Y.Sun. *Phys. Rev. B*, **73**, 064302 (2006)
55. J.T.Last. *Phys. Rev.*, **105**, 1740 (1957)
56. Ph. Colomban. *Ann. Chim. Sci. Matér.*, **24**, 1 (1999)
57. M.Karlsson, A.Matic, C.S.Knee, I.Ahmed, S.G.Eriksson, L.Börjesson. *Chem. Mater.*, **20**, 3480 (2008)
58. M.Glerup, F.W.Poulsen, R.W.Berg. *Solid State Ion.*, **148**, 83 (2002)
59. M.Karlsson, A.Matic, S.F.Parker, I.Ahmed, L.Börjesson, S.Eriksson. *Phys. Rev. B*, **77**, 104302 (2008)
60. A.Slodczyk, P.Colomban, D.Lamago, M.-H.Limage, F.Romain, S.Willemin, B.Sala. *Ionics*, **14**, 215 (2008)
61. M.Karlsson, I.Ahmed, A.Matic, S.G.Eriksson. *Solid State Ion.*, **181**, 126 (2010)
62. A.Perrichon, N.Torino, E.Jedvik Granhed, Y.-C.Lin, S.F.Parker, M.Jiménez-Ruiz, M.Karlsson, P.F.Henry. *J. Phys. Chem. C*, **124**, 8643 (2020)
63. K.Nakamoto, M.Margoshes, R.E.Rundle. *J. Am. Chem. Soc.*, **77**, 6480 (1955)
64. M.Karlsson, A.Matic, E.Zanghellini, I.Ahmed. *J. Phys. Chem. C*, **114**, 6177 (2010)
65. C.W.Mburu, S.M.Gaita, C.S.Knee, M.J.Gatari, M.Karlsson. *J. Phys. Chem. C*, **121**, 16174 (2017)
66. H.Yugami, Y.Shibayama, S.Matsuo, M.Ishigame, S.Shin. *Solid State Ion.*, **85**, 319 (1996)
67. M.Karlsson, M.E.Björketun, P.G.Sundell, A.Matic, G.Wahnström, D.Engberg, L.Börjesson, I.Ahmed, S.Eriksson, P.Berastegui. *Phys. Rev. B*, **72**, 094303 (2005)
68. K.Arai, M.Saito, K.Suganami, M.Inada, K.Hayashi, T.Motohashi. *J. Solid State Chem.*, **308**, 122913 (2022)
69. A.Zhu, G.Zhang, T.Wan, T.Shi, H.Wang, M.Wu, C.Wang, S.Huang, Y.Guo, H.Yu, Z.Shao. *Electrochim. Acta*, **259**, 559 (2018)
70. A.Slodczyk, P.Colomban, O.Zaafarani, O.Lacroix, J.Loricourt, F.Grasset, B.Sala. *MRS Proc.*, **1309**, 1013090321 (2011)
71. *Proton Conductors: Solids, Membranes and Gels — Materials and Devices*. (Ed. P.Colomban). (Cambridge: Cambridge University Press, 1992); <https://www.cambridge.org/core/books/proton-conductors/1C3694D84D4FFD205D875B30E3800AE0>
72. Ph.Colomban, J.Tomkinson. *Solid State Ion.*, **97**, 123 (1997)
73. N.A.Tarasova, A.O.Galisheva, I.E.Animitsa, D.V.Korona. *Russ. J. Phys. Chem. A*, **94**, 818 (2020)
74. Y.D.Zhang, A.K.Zhu, Y.M.Guo, C.C.Wang, M.Ni, H.Yu, C.H.Zhang, Z.P.Shao. *Appl. Energy*, **238**, 344 (2019)
75. I.Ahmed, S.-G.Eriksson, E.Ahlberg, C.S.Knee, P.Berastegui, L.-G.Johansson, H.Rundlöf, M.Karlsson, A.Matic, L.Börjesson, D.Engberg. *Solid State Ion.*, **177**, 1395 (2006)
76. P.Du, Q.Chen, Z.Fan, H.Pan, F.G.Haibach, M.A.Gomez, A.Braun. *Commun. Phys.*, **3**, 1 (2020)
77. S.Upasen, P.Batocchi, F.Mauvy, A.Slodczyk, P.Colomban. *Ceram. Int.*, **41**, 14137 (2015)
78. H.P.Ding, W.Wu, C.Jiang, Y.Ding, W.J.Bian, B.X.Hu, P.Singh, C.J.Orme, L.C.Wang, Y.Y.Zhang, D.Ding. *Nat. Commun.*, **11**, 1907 (2020)
79. N.Bork, K.E.J.Eurenius, J.Rossmeisl, C.S.Knee, T.Vegge. *J. Appl. Phys.*, **112**, 033705 (2012)
80. M.Huse, A.W.B.Skilbred, M.Karlsson, S.G.Eriksson, T.Norby, R.Haugsrud, C.S.Knee. *J. Solid State Chem.*, **187**, 27 (2012)
81. I.Animitsa, T.Denisova, A.Neiman, A.Nepryahin, N.Kochetova, N.Zhuravlev, Ph. Colomban. *Solid State Ion.*, **162–163**, 73 (2003)
82. N.Tarasova, I.Animitsa, T.Denisova, R.Nevmyvako. *Solid State Ion.*, **275**, 47 (2015)
83. N.Tarasova, Ph.Colomban, I.Animitsa. *J. Phys. Chem. Solids*, **118**, 32 (2018)
84. T.Scherban, A.S.Nowick. *Solid State Ion.*, **35**, 189 (1989)
85. K.D.Kreuer. *Annu. Rev. Mater. Res.*, **33**, 333 (2003)
86. J.Bielecki, S.F.Parker, L.Mazzei, L.Börjesson, M.Karlsson. *J. Mater. Chem. A*, **4**, 1224 (2016)
87. A.Perrichon, M.Jiménez-Ruiz, L.Mazzei, S.M.H.Rahman, M.Karlsson. *J. Mater. Chem. A*, **7**, 17626 (2019)
88. J.Gao, Y.Meng, J.H.Duffy, K.S.Brinkman. *Adv. Energy Sustain. Res.*, **2**, 2100098 (2021)
89. B.Hua, Y.-F.Sun, M.Li, N.Yan, J.Chen, Y.-Q.Zhang, Y.Zeng, B.Shalchi Amirkhiz, J.-L.Luo. *Chem. Mater.*, **29**, 6228 (2017)
90. A.Grimaud, J.M.Bassat, F.Mauvy, P.Simon, A.Canizares, B.Rousseau, M.Marrony, J.C.Grenier. *Solid State Ion.*, **191**, 24 (2011)

91. A.Slodczyk, P.Colomban, S.Willemin, O.Lacroix, B.Sala. *J. Raman Spectrosc.*, **40**, 513 (2009)
92. K.D.Kreuer, S.Adams, W.Munch, A.Fuchs, U. Klock, J.Maier. *Solid State Ion.*, **145**, 295 (2001)
93. A.Slodczyk, M.-H.Limage, P.Colomban, O.Zafrani, F.Grasset, J.Loricourt, B.Sala. *J. Raman Spectrosc.*, **42**, 2089 (2011)
94. L.Boyer, B.Piriou, J.Carpena, J.L.Lacout. *J. Alloys Compd.*, **311**, 143 (2000)
95. Ph.Colomban. *J. Mol. Struct.*, **270**, 407 (1992)
96. M.Karlsson. *Dalton Trans.*, **42**, 317 (2012)
97. L.Malavasi, C.Ritter, G.Chiodelli. *Chem. Mater.*, **20**, 2343 (2008)
98. S.T.Norberg, S.Hull, I.Ahmed, S.G.Eriksson, D.Marrocchelli, P.A.Madden, P.Li, J.T.S.Irvine. *Chem. Mater.*, **23**, 1356 (2011)
99. D.Noferini, M.M.Koza, G.J.Nilsen, M.Karlsson. *Solid State Ion.*, **324**, 163 (2018)
100. J.G.Lee, A.B.Naden, C.D.Savani, P.A.Connor, J.L.Payne, J.M.Skelton, A.S.Gibbs, J.Hui, S.C.Parker, J.T.S.Irvine. *Adv. Energy Mater.*, **11**, 2101337 (2021)
101. F.G.Kinyanjui, S.T.Norberg, I.Ahmed, S.G.Eriksson, S.Hull. *Solid State Ion.*, **225**, 312 (2012)
102. *NIST* (2011); <https://www.nist.gov/laboratories/tools-instruments/prompt-gamma-ray-activation-analysis-pgaa>
103. C.Y.Jones, J.Wu, L.Li, S.M.Haile. *J. Appl. Phys.*, **97**, 114908 (2005)
104. C.Karmonik, T.J.Udovic, R.L.Paul, J.J.Rush, K.Lind, R.Hempelmann. *Solid State Ion.*, **109**, 207 (1998)
105. A.Perrichon, E.Jedvik Granhed, G.Romanelli, A.Piovano, A.Lindman, P.Hyldgaard, G.Wahnström, M.Karlsson. *Chem. Mater.*, **32**, 2824 (2020)
106. L.Malavasi, H.Kim, T.Proffen. *J. Appl. Phys.*, **105**, 123519 (2009)
107. Q.Chen, J.Banyte, X.Zhang, J.P.Embs, A.Braun. *Solid State Ion.*, **252**, 2 (2013)
108. P.Colomban, A.Slodczyk, D.Lamago, G.Andre, O.Zafrani, O.Lacroix, S.Willemin, B.Sala. *J. Phys. Soc. Jpn.*, **79**, 1 (2010)
109. T.Springer. In *Springer Tracts in Modern Physics. Vol. 64*. (Ed. T.Springer) (Heidelberg: Springer. Berlin, 1972). P.1; <https://doi.org/10.1007/BFb0042411>
110. L.Malavasi, H.Kim, T.Proffen. *ChemPhysChem*, **9**, 2309 (2008)
111. A.K.Eriksson Andersson, S.M.Selbach, T.Grande, C.S.Knee. *Dalton Trans.*, **44**, 10834 (2015)
112. M.Karlsson, A.Matic, D.Engberg, M.E.Björketun, M.M.Koza, I.Ahmed, G.Wahnström, L.Börjesson, S.-G.Eriksson. *Solid State Ion.*, **180**, 22 (2009)
113. M.Pionke, T.Mono, W.Schweika, T.Springer, H.Schober. *Solid State Ion.*, **97**, 497 (1997)
114. L.Mazzei, A.Perrichon, A.Mancini, G.Wahnström, L.Malavasi, S.F.Parker, L.Börjesson, M.Karlsson. *J. Mater. Chem. A*, **7**, 7360 (2019)
115. A.Slodczyk, P.Colomban, N.Malikova, O.Zafrani, S.Longeville, J.-M.Zanotti, O.Lacroix, B.Sala. *Solid State Ion.*, **252**, 7 (2013)
116. E.Kendrick, K.S.Knight, M.S.Islam, P.R.Slater. *Solid State Ion.*, **178**, 943 (2007)
117. J.F.Basbus, M.D.Arce, J.A.Alonso, M.A.González, G.J.Cuello, M.T.Fernández-Díaz, Z.Sha, S.J.Skinner, L.V.Mogni, A.C.Serquis. *J. Mater. Chem. A*, **10**, 9037 (2022)
118. C.Eklöf-Österberg, L.Mazzei, E.J.Granhed, G.Wahnström, R.Nedumkandathil, U. Häussermann, A.Jaworski, A.J.Pell, S.F.Parker, N.H.Jalarvo, L.Börjesson, M.Karlsson. *J. Mater. Chem. A*, **8**, 6360 (2020)
119. E.J.Granhed, A.Lindman, C.Eklöf-Österberg, M.Karlsson, S.F.Parker, G.Wahnström. *J. Mater. Chem. A*, **7**, 16211 (2019)
120. X.Liu, T.S.Bjørheim, R.Haugsrud. *J. Mater. Chem. A*, **5**, 1050 (2017)
121. J.Bielecki, S.F.Parker, D.Ekanayake, S.M.H.Rahman, L.Börjesson, M.Karlsson. *J. Mater. Chem. A*, **2**, 16915 (2014)
122. L.Mazzei, A.Perrichon, A.Mancini, L.Malavasi, S.F.Parker, L.Börjesson, M.Karlsson. *J. Phys. Chem. C*, **123**, 26065 (2019)
123. M.A.Gomez, D.L.Fry, M.E.Sweet, M.A.Gomez, D.L.Fry, M.E.Sweet. *J. Korean Ceram. Soc.*, **53**, 521 (2016)
124. T.Nakamura, R.Oike, Y.Ling, Y.Tamenori, K.Amezawa. *Phys. Chem. Chem. Phys.*, **18**, 1564 (2016)
125. F.Giannici, M.Shirpour, A.Longo, A.Martorana, R.Merkle, J.Maier. *Chem. Mater.*, **23**, 2994 (2011)
126. F.Giannici, A.Longo, A.Balerna, K.-D.Kreuer, A.Martorana. *Chem. Mater.*, **19**, 5714 (2007)
127. A.Longo, F.Giannici, A.Balerna, C.Ingrao, F.Deganello, A.Martorana. *Chem. Mater.*, **18**, 5782 (2006)
128. F.Giannici, A.Longo, A.Balerna, A.Martorana. *Chem. Mater.*, **21**, 597 (2009)
129. D.Han, P.Zhong, X.Zhang, L.Jiang. *J. Mater. Chem. A*, **10**, 8887 (2022)
130. N.Wang, S.Hinokuma, T.Ina, C.Zhu, H.Habazaki, Y.Aoki. *J. Mater. Chem. A*, **8**, 11043 (2020)
131. S.Ricote, N.Bonanos, G.Caboche. *Solid State Ion.*, **180**, 990 (2009)
132. C.Kjølseth, L.-Y.Wang, R.Haugsrud, T.Norby. *Solid State Ion.*, **181**, 1740 (2010)
133. D.K.Lim, H.N.Im, S.J.Song, H.I.Yoo. *Sci. Rep.*, **7**, 486 (2017)
134. R.Z.Ren, Z.H.Wang, C.M.Xu, W.Sun, J.S.Qiao, D.W.Rooney, K.N.Sun. *J. Mater. Chem. A*, **7**, 18365 (2019)
135. C.C.Duan, J.H.Tong, M.Shang, S.Nikodemski, M.Sanders, S.Ricote, A.Almansoori, R.O'Hayre. *Science*, **349**, 1321 (2015)
136. R.Strandbakke, V.A.Cherepanov, A.Y.Zuev, D.S.Tsvetkov, C.Argiris, G.Sourkouni, S.Prünke, T.Norby. *Solid State Ion.*, **278**, 120 (2015)
137. Y.Zhou, M.Shiraiwa, M.Nagao, K.Fujii, I.Tanaka, M.Yashima, L.Baque, J.F.Basbus, L.V.Mogni, S.J.Skinner. *Chem. Mater.*, **33**, 2139 (2021)
138. Y.Wang, A.Chesnaud, E.Bevillon, G.Dezanneau. *Solid State Ion.*, **214**, 45 (2012)
139. T.Miruszewski, K.Dzierzgowski, P.Winiarz, D.Jaworski, K.Wiciak-Pawłowska, W.Skubida, S.Wachowski, A.Mielewczyk-Gryń, M.Gazda. *RSC Adv.*, **11**, 19570 (2021)
140. T.S.Bjørheim, S.M.H.Rahman, S.G.Eriksson, C.S.Knee, R.Haugsrud. *Inorg. Chem.*, **54**, 2858 (2015)
141. Y.H.Ling, H.Chen, J.Niu, F.Wang, L.Zhao, X.M.Ou, T.Nakamura, K.Amezawa. *J. Eur. Ceram. Soc.*, **36**, 3423 (2016)
142. I.A.Zvonareva, A.V.Kasyanova, A.P.Tarutin, G.K.Vdovin, J.G.Lyagaeva, D.A.Medvedev. *J. Am. Ceram. Soc.*, **105**, 2105 (2021)
143. N.Wang, H.Toriumi, Y.Sato, C.Tang, T.Nakamura, K.Amezawa, S.Kitano, H.Habazaki, Y.Aoki. *ACS Appl. Energy Mater.*, **4**, 554 (2020)
144. E.Fabbri, L.Bi, H.Tanaka, D.Pergolesi, E.Traversa. *Adv. Funct. Mater.*, **1**, 158 (2011)
145. K.Leonard, Y.-S.Lee, Y.Okuyama, K.Miyazaki, H.Matsumoto. *Int. J. Hydrog. Energy*, **42**, 3926 (2017)
146. W.Acuña, J.F.Tellez, M.A.Macias, P.Roussel, S.Ricote, G.H.Gauthier. *Solid State Sci.*, **71**, 61 (2017)
147. Y.Zhou, E.Liu, Yu.Chen, Y.Liu, L.Zhang, W.Zhang, Z.Luo, N.Kane, B.Zhao, L.Soule, Y.Niu, Y.Ding, H.Ding, D.Ding, M.Liu. *ACS Energy Lett.*, **6**, 1511 (2021)
148. S.Choi, C.J.Kucharczyk, Y.G.Liang, X.H.Zhang, I.Takeuchi, H.I.Ji, S.M.Haile. *Nat. Energy*, **3**, 202 (2018)
149. R.Z.Ren, Z.H.Wang, X.G.Meng, X.H.Wang, C.M.Xu, J.S.Qiao, W.Sun, K.N.Sun. *ACS Appl. Energy Mater.*, **3**, 4914 (2020)
150. N.Tarasova, A.Galisheva, I.Animitsa, K.Belova. *Materials*, **14** (2021)
151. A.Chesnaud, M.D.Brida, S.Estradé, F.Peiró, A.Tarancón, A.Morata, G.Dezanneau. *J. Eur. Ceram. Soc.*, **35**, 3051 (2015)

152. D.L.Han, Y.Okumura, Y.Nose, T.Uda. *Solid State Ion.*, **181**, 16016 (2010)
153. R.Zohourian, R.Merkle, J.Maier. *Solid State Ion.*, **299**, 64 (2017)
154. A.S.Farlenkov, L.P.Putilov, M.V.Ananyev, E.P.Antonova, V.A.Eremin, A.Y.Stroeva, E.A.Sherstobitova, V.I.Voronin, I.F.Berger, V.I.Tsidilkovski, V.P.Gorelov. *Solid State Ion.*, **306**, 126 (2017)
155. D.L.Han, N.Hatada, T.Uda, R.Koc. *J. Am. Ceram. Soc.*, **99**, 3745 (2016)
156. Y.Adachi, N.Hatada, T.Uda. *Int. J. Hydrog. Energy*, **41**, 21450 (2016)
157. D.Hashimoto, D.Han, T.Uda. *Solid State Ion.*, **262**, 687 (2014)
158. R.Sažinas, M.-A.Einarsrud, T.Grande. *J. Mater. Chem. A*, **5**, 5846 (2017)
159. T.S.Bjørheim, M.F.Hoedl, R.Merkle, E.A.Kotomin, J.Maier. *J. Phys. Chem. C*, **124**, 1277 (2019)
160. Y.Huang, R.Merkle, J.Maier. *J. Mater. Chem. A*, **9**, 14775 (2021)
161. M.Dippon, S.M.Babiniec, H.Ding, S.Ricote, N.P.Sullivan. *Solid State Ion.*, **286**, 117 (2016)
162. T.Kuroha, K.Yamauchi, Y.Mikami, Y.Tsuji, Y.Niina, M.Shudo, G.Sakai, N.Matsunaga, Y.Okuyama. *Int. J. Hydrog. Energy*, **45**, 3123 (2020)
163. C.Zhou, X.Shen, D.Liu, J.Cui, Y.Yi, M.Fei, J.Zhou, L.Zhang, R.Ran, M.Xu, W.Zhou, Z.Shao. *J. Power Sources*, **530**, 231321 (2022)
164. F.He, Z.Y.Teng, G.M.Yang, C.Zhou, D.Q.Guan, S.H.Chen, R.Ran, W.Wang, W.Zhou, Z.P.Shao. *J. Power Sources*, **460**, 228105 (2020)
165. W.Wang, Y.Chen, F.Wang, M.O.Tade, Z.Shao. *Chem. Eng. Sci.*, **126**, 22 (2015)
166. W.Wang, C.Su, R.Ran, B.Zhao, Z.Shao, M.O.Tade, S.Liu. *ChemSusChem*, **7**, 1719 (2014)
167. L.Szentmiklósi, T.Belgya, Z.Révay, Z.Kis. *J. Radioanal. Nucl. Chem.*, **286**, 501 (2010)